Response to the Reviewers

Manuscript No.: egusphere-2026-1311

Title: Simulating the impacts of utility-scale photovoltaic installations with a physically based coupled WRF-PV model

Dear Topic Editor and Reviewers,

We sincerely thank the topic editor and the reviewers for their careful evaluation of our manuscript and for their valuable and constructive comments. We have revised the manuscript accordingly and provide detailed point-by-point responses below. The original reviewer comments are shown in *blue italics*, followed by our corresponding responses and the revised text. We hope that our revisions and responses have adequately addressed the reviewers' comments and concerns.

Thank you again for your time and valuable comments.

Yours sincerely,

Yiran Chen, Jiming Jin, and Yimin Liu

on behalf of all authors

CONTENTS

Response to Reviewer 1

This study couples a physically based PV-panel energy-balance model (an adaptation of Heusinger et al., 2020) into the Noah land-surface module in the WRF model, deriving a combined PV-ground energy-balance equation that ensures closure between panels, ground, and atmosphere. Coupled model simulations with and without PV modules are done over a major utility-scale PV deployment region in northwestern China for the summers of 2018-2024 and compared against available observations. The authors report a daytime cooling of skin temperature, a daytime warming of 2 m air temperature, enhanced sensible heat flux, weakened lower-tropospheric stability, increased low-level cloud, and a redistribution of summer precipitation toward extremes.

The manuscript addresses physically consistent representation of utility-scale PV installations in regional climate models, a topic of clear relevance to GMD readers. The energy-closed coupling formulation is a reasonable contribution to the modeling side of PV modules' climate effect. I have a few general concerns on incomplete implementation details described in the methodology section, significance of the model validation results, and how it differentiates from the previous modeling studies. Overall, I would recommend a major revision before publication.

Response: We sincerely thank you for your valuable comments and constructive suggestions. We have substantially revised the manuscript to address all the concerns raised in the review. First, we expanded the methodology section by adding further details on the model formulation, numerical implementation, configurable parameters, and coupling with the land-surface model. Second, we refined the WRF physical parameterization configuration by adopting the vegetation-dependent scheme for surface thermal roughness length over land and repeated the simulations. The revised configuration improved the baseline performance of WRF_CTL, while the inclusion of the PV coupling scheme further improved the simulation performance. We also updated the reanalysis dataset used for model evaluation by adopting the higher-resolution CLDAS dataset at a spatial resolution of 0.0625°. Third, we clarified the distinction between WRF-PV and previous modeling approaches by conducting an additional effective albedo experiment and directly comparing the different implementations. We redrew all the figures and repeated the diagnostic analyses, although the PV-induced effects were similar to those in the previous version. Detailed responses to each of these concerns are provided below.

General Suggestions 1: *Although I understand that this study incorporates two-way coupling and atmosphere-panel- surface energy closure, which is a valuable addition to the previous models, these changes seem incremental and are not shown to bring significant improvement to the model performance. Specifically:*

General Suggestions 1-1: *Section 4.1 serves as validation of the model implementation. However, the comparison mainly focuses on regional mean, and the difference between the PV run and the control run is so small that I doubt whether it is noise from internal variability. From my expectation,* *I would see larger difference when averaged only over PV regions. In this case, how is the model-simulated T and precipitation compared to the observed ones?*

Response: Thank you for this important comment. We additionally evaluated T2 and precipitation on the CLDAS reanalysis grids over PV installations. WRF_PV produced a T2 bias of +1.72 °C and an RMSE of 2.40 °C, compared with +1.64 °C and 2.47 °C, respectively, in WRF_CTL. The comparable positive biases in WRF_PV and WRF_CTL suggest that the absolute warm bias may largely reflect systematic biases shared by both WRF simulations. For precipitation, WRF_PV produced a bias of −0.01 mm day^{-1} and an RMSE of 0.661 mm day^{-1}, compared with +0.05 mm day^{-1} and 0.735 mm day^{-1} in WRF_CTL. Thus, WRF_PV showed a precipitation bias closer to zero and a lower RMSE over the PV regions. Please note that the evaluation in Section 4.1 was based on 0.0625° CLDAS grid cells containing PV installations, whereas the differences between WRF_PV and WRF_CTL in Section 4.2 were calculated over the 3 km WRF PV grid cells. Figures R1.1 and R1.2 compare the responses over the entire D03 domain and WRF PV grid cells. The T2 response was substantially stronger over the PV grid cells (Fig. R1.1). At each hour of the diurnal cycle, the WRF_PV minus WRF_CTL difference from each day was treated as one sample, and a t-test was used to determine whether the mean difference was significantly different from zero. The precipitation frequency distribution showed larger differences over the PV grid cells (Fig. R1.2).

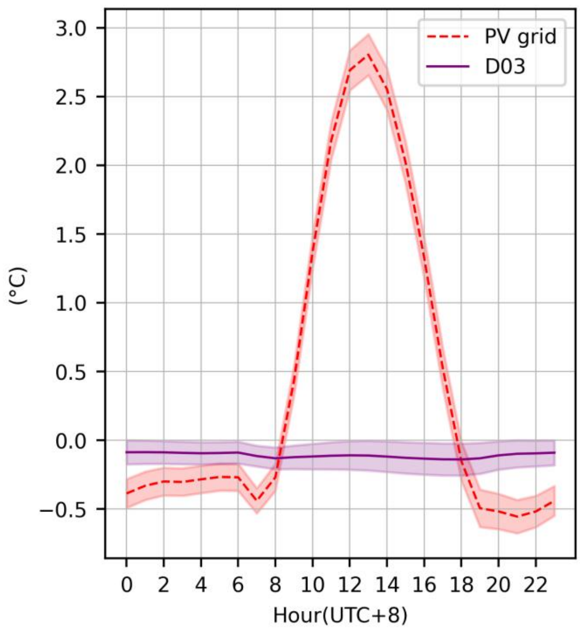

Figure R1.1: Mean diurnal cycle of the WRF_PV–WRF_CTL difference in 2 m air temperature (T2, °C) averaged over D03 and WRF PV grid cells during the summers of 2018–2024. Shaded areas represent the 95 % confidence intervals based on mean ± 1.96 × standard error.

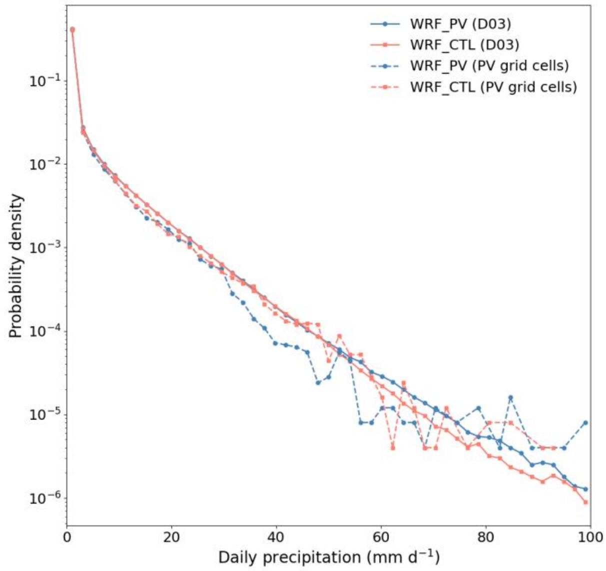

Figure R1.2: Probability density distributions of daily precipitation intensity in WRF_PV and WRF_CTL over D03 and WRF PV grid cells during the summers of 2018–2024. Solid and dashed lines represent the D03 and PV grid cells, respectively.

The revised text reads:

> "Over the entire D03 domain, WRF_PV produced a mean bias of +0.38 °C and an RMSE of 1.78 °C, compared with +0.49 °C and 1.81 °C, respectively, for WRF_CTL. On the CLDAS grid cells over PV installations, WRF_PV produced a mean bias of +1.72 °C and an RMSE of 2.40 °C, whereas WRF_CTL produced corresponding values of +1.64 °C and 2.47 °C."
>
> "Over the entire D03 domain, WRF_PV produced a mean bias of +0.08 mm and an RMSE of 0.548 mm, compared with +0.05 mm and 0.549 mm, respectively, for WRF_CTL. On the CLDAS grid cells over PV installations, WRF_PV produced a mean bias of −0.01 mm and an RMSE of 0.661 mm, whereas WRF_CTL produced corresponding values of +0.05 mm and 0.735 mm."

Location: Sections 4.1.1 and 4.1.2, lines 248–251, 266–269; Figs. 2–3.

General Suggestions 1-2: *While section 4.1.3 presents simulated skin temperature compared against MODIS- observed skin temperature only over the PV grid cells, the difference of the probability distribution is still very small, and there are still a substantial number of samples that have very large bias above 5 K.*

Response: Thank you for this helpful comment. In response to your suggestion, we refined the physical parameterization configuration and repeated the simulations. Figure R1.3 shows that TSK errors in WRF_PV are more concentrated near zero, whereas WRF_CTL is shifted toward positive errors. The relatively large errors in some individual samples may arise from differences in the timing and representation of short-term weather processes, because skin temperature responds rapidly to changes in cloudiness and surface solar heating (Wang et al., 2014; Trigo et al., 2015). Such differences can produce large errors at individual MODIS overpass times. We also added an analysis of the mean bias values and recalculated the evaluation statistics by first averaging TSK over all PV grid cells at each MODIS observation time and then calculating the statistics across the 77 observation times. WRF_CTL showed a mean bias of +0.697 °C and an RMSE of 3.071 °C, whereas WRF_PV showed a mean bias of −0.340 °C and an RMSE of 2.560 °C. Thus, WRF_PV reduced the RMSE by

0.511 °C and decreased the magnitude of the mean bias. These results indicate improved agreement with MODIS for TSK over the PV installations.

The revised text reads:

> "A total of 10,310 valid 8-day MODIS–WRF collocations were retained and used to construct the error distributions shown in Fig. 4. The WRF_PV errors were more concentrated near zero, whereas the WRF_CTL distribution was shifted toward positive errors. At each observation time, MODIS LST and WRF TSK were first averaged over all valid PV grid cells. Bias and RMSE were then calculated from the 77 paired time-mean samples. WRF_CTL produced a mean bias of +0.697 °C and an RMSE of 3.071 °C, whereas WRF_PV produced a mean bias of −0.340 °C and an RMSE of 2.560 °C. Thus, WRF_PV reduced the RMSE by 0.511 °C and reduced the magnitude of the mean bias relative to WRF_CTL. These results indicate that WRF_PV achieved better agreement with MODIS than WRF_CTL over the PV installations."

Location: Section 4.1.3, lines 288–295; Fig. 4.

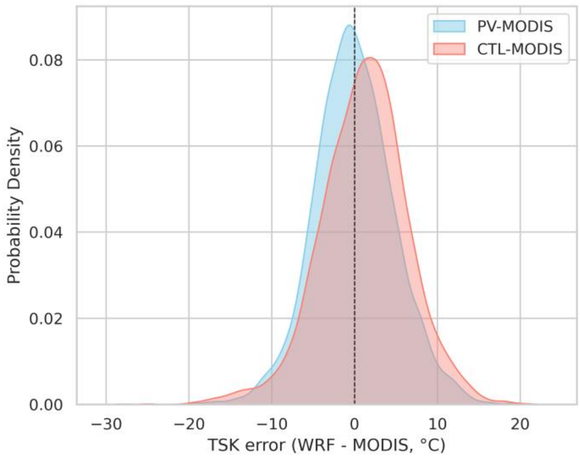

Figure R1.3: Probability density distributions of skin temperature (TSK, °C) errors for the WRF_PV (blue shade) and WRF_CTL (red shade) simulations with respect to MODIS observations. The vertical dashed line denotes zero error. (Figure 4 in the revised manuscript)

General Suggestions 1-3: *Sections 4.2~4.4 proceeds to analyze impacts on temperature, local energy budget, and atmospheric responses. I appreciate it to include physical interpretation of the model results. However, previous modeling work also has similar analyses, and such decomposition in this study is not accompanied by in-situ measurements as validation. Is the simulated PV module temperature consistent with the real world scenario?*

Response: Thank you for this important comment. We agree that collocated in situ measurements of PV module temperature and surface energy fluxes would provide direct validation. However, corresponding measurements were not available for the multiple PV farms and simulation periods considered in this regional study. Nevertheless, the UCRC-Solar model underlying WRF-PV has previously been evaluated against measured module temperature and power production (Heusinger et al., 2020). For comparison, Li et al. (2023) reported that the observed July mean diurnal cycle of PV module temperature at a desert PV plant in western China reached a daytime maximum of approximately 48 °C. This observed maximum is close to our simulated peak of 49 °C. The simulated increase in sensible heat flux and decreases in latent heat flux and ground heat flux are also qualitatively consistent with the field observations reported by Broadbent et al. (2019) and Jiang et al. (2021). We therefore consider the simulated PV module temperature and energy-partitioning responses to be consistent with the findings of previous field observational studies. We have added a discussion of the lack of direct site-specific measurements in this study.

The revised text reads:

> "Collocated in situ measurements of PV module temperature and surface energy fluxes were unavailable for the multiple PV farms and simulation periods considered in this regional study. However, the UCRC-Solar model underlying WRF-PV has previously been evaluated against measured module temperature and power production (Heusinger et al., 2020). In addition, the simulated peak PV module temperature of approximately 49 °C was close to the observed July daytime maximum of approximately 48 °C reported for a desert PV plant in western China (Li et al., 2023), while the simulated changes in sensible, latent, and ground heat fluxes were qualitatively consistent with previous field observations (Broadbent et al., 2019; Jiang et al., 2021). Future evaluation would benefit from broader field observations of module and near-surface air temperatures, surface energy fluxes, and power output to better constrain the energy partitioning represented by WRF-PV."

Location: Section 5, lines 485–492.

General Suggestions 1-4: *What is the expected primary benefit of introducing the two-way coupling mechanism that previous modeling studies do not possess? It would be interesting to compare the results of different implementations (including effective albedo method in Li et al., 2018) side by side and see how large the difference is.*

Response: Thank you for this important comment. The primary benefit of the two-way coupling is that it dynamically represents the interactions among PV panels, the underlying ground, and the atmosphere. Atmospheric conditions affect panel temperature and power generation, while the panels modify surface radiation, shading, and heat exchanges, which subsequently feed back to the near-surface atmosphere. This differs from the effective albedo method, which represents PV installations through a prescribed bulk albedo and does not explicitly account for panel thermal properties, shading, or panel–ground energy exchanges.

Following this suggestion, we conducted an additional WRF_EA experiment using the effective albedo formulation of Li et al. (2018), while retaining the same domain, simulation period, and physical configuration as WRF_PV and WRF_CTL, and using the same PV spatial distribution as WRF_PV. A constant effective albedo of 0.15 was prescribed for all PV grid cells. The experimental design, effective albedo formulation, and evaluation results have been added to Section 5, Supplementary Text S2 and Table S1, and the three experiments are now compared side by side. The comparison shows that the overestimation associated with WRF_EA was most evident in TSK over PV installations and in domain-scale precipitation. WRF_EA produced a mean TSK bias of +2.62 °C and an RMSE of 4.02 °C, both larger than those of WRF_PV (−0.34 and 2.56 °C) and WRF_CTL (+0.70 and 3.07 °C). Its precipitation bias and RMSE were +0.14 and 1.06 mm day^{-1}, respectively, compared with WRF_PV (+0.08 and 0.55 mm day^{-1}) and WRF_CTL (+0.05 and 0.55 mm day^{-1}) (Table R1.1). Relative to WRF_CTL, WRF_EA increased TSK, whereas WRF_PV produced daytime TSK cooling, which is more consistent with satellite-based observations. The domain-scale T2 bias was comparable among the three experiments, although the T2 RMSE was larger in WRF_EA. We therefore do not interpret the effective albedo method as producing uniformly stronger responses across all variables. We have therefore revised the manuscript to clarify both the expected benefit of the two-way coupling and the directly supported differences among the three implementations.

The revised text reads:

"To compare WRF-PV with the effective albedo (EA) method of Li et al. (2018), we conducted an additional experiment (WRF_EA) in which the WRF-PV scheme was replaced by the EA method. The model domain, simulation period, and physical configuration remained unchanged. Details of the experimental design and the complete evaluation results are provided in Supplementary Text S2. WRF_EA produced a mean TSK bias of +2.62 °C and an RMSE of 4.02 °C, both larger than those of WRF_PV (−0.34 and 2.56 °C) and WRF_CTL (+0.70 and 3.07 °C). Relative to WRF_CTL, WRF_EA increased TSK, whereas WRF_PV produced daytime surface cooling. The warming simulated by WRF_EA contrasts with the daytime cooling reported by previous satellite-based studies of utility-scale PV farms (Zhang and Xu, 2020; Fan and Huang, 2021; Li et al., 2021; Wang et al., 2024; Xu et al., 2024). These contrasting responses highlight the limitations of representing PV installations solely through the bulk albedo of the entire grid cell. The EA method does not account for shading and the associated changes in ground heat storage. By contrast, WRF-PV explicitly represented panel coverage, panel thermal properties, and shading effects, and showed closer agreement with MODIS."

Location: Section 5, lines 470–480; Supplementary Text S2 and Table S1.

Table R1.1: Evaluation statistics for WRF_CTL, WRF_PV, and WRF_EA during the summers of 2018–2024. (Table S1 in the supplement)

Variable and evaluation range	Experiment	Bias	RMSE
Panel TSK versus MODIS	WRF_CTL	+0.697 °C	3.071 °C
	WRF_PV	−0.340 °C	2.560 °C
	WRF_EA	+2.619 °C	4.021 °C
T2 versus CLDAS	WRF_CTL	+0.49 °C	1.81 °C
	WRF_PV	+0.38 °C	1.78 °C
	WRF_EA	+0.40 °C	2.22 °C
precipitation versus CLDAS	WRF_CTL	+0.05 mm day^{-1}	0.55 mm day^{-1}
	WRF_PV	+0.08 mm day^{-1}	0.55 mm day^{-1}
	WRF_EA	+0.14 mm day^{-1}	1.06 mm day^{-1}

General Suggestions 2: *Since this is a manuscript submitted to GMD, I would expect a complete and detailed model description. In its current form, the manuscript is missing a few important pieces. A rule of thumb is that readers should be able to reproduce the results from reading the methodology section, even when the model is open source. Some notable examples are listed below, while more can be found in the specific points:*

General Suggestions 2-1: *The authors in many cases point the readers to previous papers. All parameters used in this study are not specified. A table that lists all configurable parameters in this module and their values is desired. Furthermore, does the model take both fixed-tilt and single-axis tracking solar farms into account? Does the model account for azimuth angle of solar panel tilt and solar radiation? Do all the identified solar farms share the same panel configurations? Please discuss the sensitivity of the results to this assumption, or at minimum acknowledge it as a limitation.*

Response: Thank you for this helpful comment. We have added a new table listing the main configurable parameters used in the WRF-PV simulations, including panel tilt angle, panel azimuth angle, module geometry, row spacing, PV coverage fraction, panel height, emissivity, conversion efficiency, and the temperature derating coefficient. In the present simulations, all PV farms were represented as fixed-tilt arrays. Single-axis tracking systems were not included. The panel azimuth angle was set to 0°, corresponding to a south-facing orientation. The model accounts for solar geometry through the incidence angle calculation, which includes the solar zenith angle and solar azimuth angle. All identified PV farms were assigned the same representative panel configuration because farm-specific installation information was not available. This simplification was supported by their location within a relatively narrow mid-latitude range with broadly similar solar geometry. We have acknowledged this simplification as a limitation in the revised manuscript.

The revised text reads:

> "Because farm-specific installation information was unavailable, all PV farms were represented as fixed-tilt arrays with the same representative panel parameters. This simplification was supported by their location within a relatively narrow mid-latitude range with broadly similar solar geometry."

Location: Sections 2.1 and 5, lines 493–495; Table 1.

Table R1.2: Configurable parameters used in the simulations (Table 1 in the revised manuscript)

Parameter	Symbol	Value	Unit	Source
Panel tilt angle	β	37	°	Jiang et al. (2021)
Panel length	L	3.3	m	Jiang et al. (2021)
PV row spacing	W_rows	7.5	m	Jiang et al. (2021)
Panel height	h	1.5	m	Jiang et al. (2021)
PV cover fraction	f_{PV}	0.35	–	Jiang et al. (2021)
Panel azimuth angle (0° = south-facing)	γ	0	°	–
Refractive index of the glazing layer	n	1.38	–	Zhang et al. (2014); Ferrari Muniz et al. (2025)
Maximum conversion efficiency	Eff_{PV}	0.16	–	Shaner et al. (2016); Heusinger et al. (2020)
Temperature derating coefficient	η	0.005	K^{-1}	Luque and Hegedus (2011); Heusinger et al. (2020)
Front PV-surface emissivity	ε_{top}	0.82	–	Heusinger et al. (2020)
Rear PV-surface emissivity	ε_{btm}	0.97	–	Heusinger et al. (2020)
Rear PV-surface albedo	$\alpha_{PV,btm}$	0.1	–	Heusinger et al. (2020)
Convective heat-transfer coefficient	h_c	$9.2e^{-0.6U}$ $+12.274U^{0.78}$	W m^{-2} K^{-1}	Heusinger et al. (2020)

General Suggestions 2-2: *In addition, Section 2.2 derives Eqs. (9)~(14) but never explains where in the land model the new equations sit. At what stage of the Noah time step are the PV fluxes computed? Are SW_dir, SW_dif and LW_down obtained from the radiation scheme of the host atmospheric column? Is the panel temperature T_PV solved diagnostically (since C_module is set to zero, per L131) or with a small numerical inertia? How is the soil- temperature equation modified given that GRDFLX is now driven by the shaded ground rather than the unshaded surface? A short numerical-implementation subsection is required.*

Response: Thank you for this helpful comment. We agree that the original manuscript did not sufficiently explain how the PV-ground coupling equations are implemented within the land surface model. We have added a numerical implementation subsection (Section 2.3) to clarify this point. In the revised manuscript, we explain that the PV scheme is implemented within the WRF surface-driver sequence, where the PV radiative and thermal fluxes are computed for PV grid cells before the land surface model calculation at each land-surface time step. We also clarify that the shortwave and longwave radiative inputs used by the PV scheme, including SW_{dir}, SW_{dif}, and LW_{down}, are obtained from the radiation scheme of the host WRF atmospheric column. Because the module heat capacity is neglected, the PV panel temperature is solved diagnostically from the steady PV energy-balance equation at each time step. We further clarify that the soil-temperature equation in the land surface model is retained. For the land surface model calculation, the radiative forcing imposed on the ground surface is modified according to the shaded-ground energy balance in Eq. (7). In this treatment, PV coverage reduces the shortwave radiation reaching the ground, and the longwave input to the ground includes both atmospheric longwave radiation and longwave emission from the PV panels. The ground heat flux (GRDFLX) is then calculated within the land surface model as part of the ground energy balance and used to update soil temperature. After the land surface model calculation, the PV grid cell skin temperature (TSK) and sensible heat flux (SH) are diagnosed from the PV panel and ground contributions.

The added subsection reads:

> "The PV scheme is implemented within the WRF surface-driver sequence and is called before the land surface model calculation at each land-surface time step. The shortwave and longwave radiative inputs used by the PV scheme, including SWdir, SWdif, and LWdown, are obtained from the radiation scheme of the host WRF atmospheric column. Because the module heat capacity is neglected, the PV panel temperature is solved diagnostically from the steady PV energy-balance equation at each time step. For the subsequent land surface model calculation, the radiative forcing imposed on the ground surface is modified according to the shaded-ground energy balance in Eq. (7). In this treatment, PV coverage reduces the shortwave radiation reaching the ground, and the longwave input to the ground includes both atmospheric longwave radiation and longwave emission from the PV panels. GRDFLX is then calculated within the land surface model as part of the ground energy balance and used to update soil temperature, while the soil-temperature equation itself is retained. After the land surface model calculation, the PV grid cell TSK and SH are diagnosed from the PV panel and ground contributions."

Location: Section 2.3, lines 168–177.

General Suggestions 3: *The motivation could be more sharply tied to GMD's scope. GMD is primarily a model- development journal. The introduction reads at present like a regional climate-impact paper that happens to develop a model along the way. I would recommend reframing the goal so that the model description and evaluation come first, with the regional impact analysis as a demonstration of capability.*

Response: Thank you for this helpful suggestion. We agree that the model-development contribution of WRF-PV was not sufficiently emphasized in the original introduction. We have therefore revised the introduction to better align the scope of GMD. The revised introduction now emphasizes the need for a physically based representation of utility-scale PV installations in regional climate models, the limitations of simplified and partially coupled PV schemes, and the model-development gap addressed by WRF-PV. We have also strengthened the model description by adding a new Section 2.3, "Numerical implementation in the land surface model", which explains how the PV scheme is implemented and coupled within the WRF land-surface calculation. These revisions place the model formulation, implementation, and evaluation at the center of the manuscript, while retaining the regional impact analysis as a demonstration of capability.

The revised text reads:

"To address these gaps, this study presents WRF-PV, a physically based and fully coupled PV–ground–atmosphere scheme implemented in the WRF model. WRF-PV maintains surface energy closure between PV panels and the ground and allows the PV-induced thermal and radiative effects to interact dynamically with the atmosphere. The coupled model was applied to northwestern China, a major utility-scale PV deployment region characterized by semi-arid and arid environments, for the summers of 2018–2024. Paired simulations with and without PV panels were evaluated against reanalysis data, satellite products, and station observations, and were further used to demonstrate the effects of PV-induced surface energy changes on near-surface meteorology and regional climate. This study provides a physically consistent modeling framework for representing utility-scale PV installations in regional climate models."

Location: Section 1, lines 89–96.

Specific Point 1: *L32~33: Please elaborate on specific "potential environmental impacts". There are papers you can refer to that specifically discuss such environmental impacts (e.g., Turney and Fthenakis, 2011). Also, it seems that this sentence seems fit better with the next paragraph.*

Response: Thank you for this helpful suggestion. We have revised this part to make the potential environmental impacts more specific and moved the sentence to the beginning of the next paragraph, where the physical changes caused by PV installations are discussed. We now specify that the relevant environmental impacts include changes in surface properties and local climate conditions, following Turney and Fthenakis (2011).

The revised text reads:

"Utility-scale PV installations may induce a range of environmental impacts, including changes in surface properties and local climate conditions (Turney and Fthenakis, 2011; Barron-Gafford et al., 2019). PV installations replace natural land cover with panel arrays and modify surface physical characteristics. Over barren land, utility-scale PV installations reduce surface albedo and enhance shortwave absorption by the panels, while panel shading decreases the downward shortwave radiation reaching the underlying ground (Armstrong et al., 2016; Fan and Huang, 2020; Yue et al., 2021; Li et al., 2022; Ying et al., 2023; Wei et al., 2024; Zhang et al., 2024). Furthermore, PV panels have a lower heat capacity than natural surfaces, causing rapid thermal responses and limited heat storage (Hasan et al., 2016)."

Location: Section 1, lines 35–41.

Specific Point 2: *L35~38: These two sentences about PV panels' shortwave effects should be joined together. All the cited studies cover both points (i.e., reduced surface albedo, greater shortwave absorption by PV panels, and reduced solar radiation reaching the ground) in the sentences.*

Response: Thank you for pointing this out. We have combined the two sentences into one sentence to describe the shortwave radiative effects of PV installations more coherently.

The revised text reads:

"Over barren land, utility-scale PV installations reduce surface albedo and enhance shortwave absorption by the panels, while panel shading decreases the downward shortwave radiation reaching the underlying ground (Armstrong et al., 2016; Fan and Huang, 2020; Yue et al., 2021; Li et al., 2022; Ying et al., 2023; Wei et al., 2024; Zhang et al., 2024)."

Location: Section 1, lines 37–40.

Specific Point 3: *L54: "Guoqing et al., 2021" the citation and the associated reference are not formatted correctly. It is using the first name instead of the last name.*

Response: Thank you for pointing this out. The citation has been revised from "Guoqing et al. (2021)" to "Li et al. (2021)", and the corresponding reference has been updated accordingly.

Specific Point 4: *L71~72: "advanced UCRC-Solar by introducing a PV canopy energy-exchange scheme" please briefly state what this scheme adds.*

Response: Thank you for this suggestion. We have revised the sentence to state that Li et al. (2024) represented PV arrays as a PV canopy and parameterized sensible heat exchange using canopy aerodynamic resistances.

The revised text reads:

> "Recent studies advanced UCRC-Solar by representing PV arrays as a canopy layer and parameterizing sensible heat exchange using canopy aerodynamic resistances (Li et al., 2024)."

Location: Section 1, lines 79–80.

Specific Point 5: *L79: How much "radiative forcing" would the utility-scale solar farms induce? In the manuscript, this is not addressed, either (see specific comments below).*

Response: Thank you for this important comment. We estimated the regional-scale magnitude of the PV-induced surface radiative perturbation by weighting the simulated perturbation by the mean fractional area of PV grid cells within D03 during 2018–2024. The PV grid cells accounted for approximately 0.464 % of the D03 grid-cell area on average, yielding an estimated daytime mean surface net-radiation perturbation of approximately +0.27 W m^{-2} over D03.

The revised text reads:

> "To estimate the regional-scale magnitude of the PV-induced surface-energy perturbation, the local flux differences over the PV grid cells were weighted by the mean fractional area of PV grid cells within D03 during 2018–2024. The PV grid cells accounted for approximately 0.464 % of the D03 grid-cell area on average. This scaling yielded estimated daytime mean D03-averaged perturbations of approximately +0.27 W m^{-2} in net radiation and +0.23 W m^{-2} in sensible heat flux. These regional-mean perturbations were substantially smaller than the corresponding local changes over the PV grid cells because PV installations occupied only a small fraction of D03."

Location: Section 4.3, lines 382–387.

Specific Point 6: *L84~85: I suggest including the time period and the geographical region of the simulations to be more specific.*

Response: Thank you for this suggestion. We have revised the sentence to specify both the simulation region and the time period.

The revised text reads:

> "The coupled model was applied to northwestern China, a major utility-scale PV deployment region characterized by semi-arid and arid environments, for the summers of 2018–2024."

Location: Section 1, lines 91–93.

Specific Point 7: *L92: "total absorbed shortwave radiation" => "total absorbed shortwave radiation by the panels"*

Response: Thank you for this suggestion. We have revised the definition of $\mathrm{SW_{tot}}$ to clarify that this term refers specifically to the total absorbed shortwave radiation by the PV panels.

Specific Point 8: *L93: "net longwave radiation exchange" => "net longwave radiation flux into the panel" (indicating that positive values mean net energy gain in the panels)*

Response: Thank you for pointing this out. We have revised the description of $\mathrm{LW_{PV}^*}$. In the revised manuscript, $\mathrm{LW_{PV}^*}$ is defined as the net longwave radiation flux into the panel, with positive values indicating a net energy gain by the panel.

Specific Point 9: *L95: "Heusinger (2021)" => "Heusinger et al. (2021)"*

Response: Thank you for noting this citation error. We have corrected the citation from "Heusinger (2021)" to "Heusinger et al. (2021)" in the revised manuscript.

Specific Point 10: *Eq. (2): A physical term-by-term explanation is desired. For example, "the first term on the RHS is direct solar radiation, where the cosine term is [...]". I am confused about the third and the fourth terms. Are they absorption by the back panel?*

Response: Thank you for this helpful suggestion. We have revised the text following Eq. (2) to provide a term-by-term physical explanation of the four shortwave-radiation components, including the meaning of each radiative component and each geometrical term. We also clarified that the third term represents ground-reflected shortwave radiation received by the front surface, whereas only the fourth term represents the ground-reflected shortwave radiation received by the rear surface.

The revised text reads:

$$\begin{aligned}\mathrm{SW_{tot}} = &\left(\mathrm{SW_{dir}} \cdot \frac{\cos\theta_h}{\cos\theta_{zh}} + \mathrm{SW_{dif}} \cdot \frac{1+\cos\beta}{2} + \mathrm{SW_{down}} \cdot \alpha_\mathrm{G} \cdot \frac{1-\cos\beta}{2}\right) \cdot \left(1-\alpha_\mathrm{PV,top}\right) \\ &+ \left(\mathrm{SW_{down}} \cdot \alpha_\mathrm{G} \cdot (1-f_\mathrm{PV}) \cdot \frac{1+\cos\beta}{2}\right) \cdot \left(1-\alpha_\mathrm{PV,btm}\right).\end{aligned} \tag{2}$$

"Eq. (2) separates $\mathrm{SW_{tot}}$ into contributions from the front and rear surfaces. $\mathrm{SW_{dir}}$, $\mathrm{SW_{dif}}$, and $\mathrm{SW_{down}}$ are the direct, diffuse, and total incoming shortwave radiation fluxes (W m^{-2}), respectively. The three terms within the first parentheses represent the shortwave radiation incident on the front surface. The first term represents direct radiation, where $\cos\theta_h / \cos\theta_{zh}$ projects the direct radiation from the horizontal plane to the tilted panel surface. θ_{zh} represents the solar zenith angle (°); θ_h is the incidence angle on the tilted panel (°). The second term represents diffuse radiation and is weighted by the unobstructed front-surface sky-view factor, $(1+\cos\beta)/2$, where β denotes the panel tilt angle (°). The third term represents ground-reflected shortwave radiation received by the front surface and is weighted by the unobstructed front-surface ground-view factor $(1-\cos\beta)/2$, where α_G is the surface albedo of the underlying ground. $\alpha_\mathrm{PV,top}$ denotes the albedo of the front PV surface, calculated from the Fresnel law as an angle-dependent reflectance. The fourth term represents ground -reflected shortwave radiation received by the rear surface of the PV panel. This component is weighted by the unobstructed view factor from the rear surface to the ground $(1+\cos\beta)/2$. $\alpha_\mathrm{PV,btm}$ denotes the albedo of the rear PV surface and is prescribed as a constant value."

Location: Section 2.1, lines 105–116.

Specific Point 11: *L100~101: "f_PV is the fractional […]" first this sentence needs grammatical correction. Also, is the "fractional surface coverage" projected to the horizontal ground? why is shaded area fraction approximated here instead of calculated analytically from angles?*

Response: Thank you for this helpful comment. We have corrected the grammar and clarified that f_{PV} denotes the horizontally projected PV panel-cover fraction. With respect to the question about why the shaded area fraction is approximated rather than calculated analytically, we agree that an analytical calculation based on solar angles and detailed panel geometry would provide a more explicit representation of shadow evolution at the scale of an individual PV farm. However, applying an analytical shadow model without adequate data would introduce additional uncertain assumptions. The present WRF-PV scheme is designed for regional climate simulations, where the model grid spacing is much larger than the row spacing of PV arrays. A fully analytical shadow calculation would require farm-specific information on panel height, panel width, row spacing, mounting height, azimuth angle, tracking system, and terrain slope. Such information is not available for all utility-scale PV installations in the regional PV dataset. For this reason, the current implementation uses a simplified shaded area fraction to represent the grid-cell-mean shading effect of PV arrays. This approximation is intended to capture the first-order reduction in shortwave radiation reaching the underlying ground, which is the process relevant for PV–ground–atmosphere energy exchange in WRF. This treatment also follows simplified PV parameterizations used in previous studies, for example Masson et al. (2014) and Salamanca et al. (2016).

Specific Point 12: *Eq. (4): Again, a brief explanation of the physical meaning of each term on the RHS would be appreciated. What is the assumption on the geometrical placement of the PV panels? Are PVF_PV the same for top panel surface and bottom panel surface?*

Response: Thank you for this helpful question. In the revised manuscript, we added a brief term-by-term explanation of Eq. (3) (renumbered from Eq. (4) in the original manuscript). We also clarified the geometrical assumption used for calculating the view factors. The view-factor calculation assumes a PV array in which panels are arranged in parallel, equally spaced rows with the same mounting height, tilt angle, and azimuth orientation. In the current implementation, the same $\mathrm{PVF}_{\mathrm{PV}}$ is used for the upper and lower panel surfaces. $\mathrm{PVF}_{\mathrm{PV}}$ represents the fraction of the view angle occupied by adjacent PV panels.

The revised text reads:

$$\begin{aligned}\mathrm{LW}^{*}_{\mathrm{PV}} = {} & \varepsilon_{\mathrm{top}} \cdot \mathrm{SVF}_{\mathrm{PV}} \cdot \mathrm{LW}_{\mathrm{down}} \\ & + \mathrm{GVF}_{\mathrm{PV}} \cdot \varepsilon_{\mathrm{G}} \cdot \sigma \cdot T_{\mathrm{G}}^{4} \\ & + \mathrm{PVF}_{\mathrm{PV}} \cdot \varepsilon_{\mathrm{top}} \cdot \sigma \cdot T_{\mathrm{PV}}^{4} + \mathrm{PVF}_{\mathrm{PV}} \cdot \varepsilon_{\mathrm{btm}} \cdot \sigma \cdot T_{\mathrm{PV}}^{4} \\ & - \varepsilon_{\mathrm{top}} \cdot \sigma \cdot T_{\mathrm{PV}}^{4} - \varepsilon_{\mathrm{btm}} \cdot \sigma \cdot T_{\mathrm{PV}}^{4},\end{aligned} \tag{3}$$

"In Eq. (3), the first term on the right-hand side represents atmospheric longwave radiation received by the front surface of the panel. The second term represents longwave radiation emitted by the ground and received by the rear surface of the panel. The third and fourth terms represent longwave radiation emitted by adjacent PV panels and received by the front and rear surfaces of the target panel, respectively. The last two terms represent longwave radiation emitted outward by the front and rear surfaces of the target panel."

Location: Section 2.1, lines 127–132.

***Specific Point 13:** Eq. (5): The authors justify the factor of two by stating that "the front and rear surfaces of the panel participate in convective heat exchange with the atmosphere". This is reasonable for free-standing bifacial panels in still air, but it is not obvious that both sides should use the same heat transfer coefficient (the rear face is partly shielded by the support structure and stands in much weaker mean wind). Please justify in more detail or reference an experimental basis.*

Response: Thank you for this helpful comment. We agree that the original wording was not sufficiently precise. We have revised the formulation and the accompanying description to avoid this implication. In the revised manuscript, the panel-air convective sensible heat exchange is expressed as:

$$Q_{H,\mathrm{PV}} = h_c(T_{\mathrm{PV}} - T_{\mathrm{A}}), \tag{4}$$

where h_c denotes the combined convective heat transfer coefficient for the exchange from the two exposed panel surfaces. This treatment follows previous studies, for example Mattei et al. (2006), Armstrong and Hurley (2010), Sun et al. (2017), and Almukhtar et al. (2023).

The revised text reads:

"where TA denotes the ambient air temperature (K). h_c denotes the combined convective heat-transfer coefficient (W m^{-2} K^{-1}) for the two exposed panel surfaces. This treatment is consistent with simplified PV thermal models that represent the two-sided panel–air convective exchange using an overall coefficient (Heusinger et al., 2020; Almukhtar et al., 2023)."

Location: Section 2.1, lines 134–136.

***Specific Point 14:** (following the comment above) Does the model consider dynamical effect of solar panels (i.e., modification to surface friction)?*

Response: Thank you for this helpful comment. The current WRF-PV implementation does not explicitly consider the dynamical effects of PV panels on surface friction. We agree that the aerodynamic effects of PV arrays may influence near-surface wind and turbulent exchange. This limitation has been clarified in the revised manuscript and will be considered in future model development.

The revised text reads:

"The current WRF-PV implementation focuses on radiative and thermal processes and does not explicitly account for the aerodynamic effects of PV arrays on surface friction, near-surface wind, and turbulent exchange."

Location: Section 5, lines 495–497.

***Specific Point 15:** Eq. (6): Here, the temperature derating uses a coefficient of 0.005 K^{-1}. Is it suitable for the PV panels examined in this study?*

Response: Thank you for this helpful comment. We agree that the temperature derating coefficient in Eq. (5) (renumbered from Eq. (6) in the original manuscript) should be expressed more generally and better justified. In the revised manuscript, we have rewritten Eq. (5) by introducing a solar conversion derating coefficient, η, as a configurable model parameter instead of embedding the numerical value in the equation. The value of η is now provided in the newly added parameter table. The value used in this study, $\eta = 0.005\ \mathrm{K}^{-1}$, is consistent with the typical range reported for silicon PV modules (Luque and Hegedus, 2011).

$$P_{\mathrm{out}} = \mathrm{SW}_{\mathrm{cell}} \cdot \mathrm{Eff}_{\mathrm{PV}} \cdot \min\left[1, 1 - \eta(T_{\mathrm{PV}} - 298.15)\right], \tag{5}$$

Specific Point 16: *Section 3.1: Please provide more details on the observational datasets. It should at least cover the spatial and temporal resolution (which the authors have stated for CMFD and NMSDC datasets), overview of the instruments or algorithms, validation results, and uncertainty.*

Response: Thank you for this helpful comment. We have expanded Section 3.1 to provide more detailed descriptions of all datasets used for model evaluation. We now report the detailed information on data production, validation, and uncertainties in Supplementary Text S1.

Specific Point 17: *L149~151: Which MODIS LST product is exactly used in this study? MODIS provides two variants ofthe surface emissivity and LST products, MOD11/MYD11 and MOD21/MYD21. They employ very different retrieval algorithms. Also what is the collocation strategy between MODIS pixels and model grid cells in derivation of Figure 5?*

Response: Thank you for this helpful comment. In the revised manuscript, the former Figure 5 has been renumbered as Figure 4. We have clarified the MODIS LST products and the collocation procedure in the revised manuscript. We used the MOD21A2 and MYD21A2 8-day daytime land surface temperature products. For spatial collocation, valid MxD21A2 pixels whose centers fell within the boundaries of the identified PV facilities were retained and assigned to the nearest WRF PV grid cell. Within each 8-day period, all retained MODIS pixels assigned to the same WRF grid cell were averaged to obtain a grid-cell-scale MODIS land surface temperature (LST) value. The corresponding daily MOD21A1D and MYD21A1D products were used to identify the valid observation dates and satellite overpass times within each 8-day period. WRF TSK was linearly interpolated to these overpass times and then averaged over the same 8-day period for comparison with the MODIS LST. The error distributions in Fig. 4 were calculated using all 10,310 valid 8-day MODIS–WRF samples at the WRF grid-cell scale.

The revised text reads:

> "The daytime LST fields from the MOD21A2 and MYD21A2 Collection 6.1 land surface temperature products were used to evaluate the simulated skin temperature (Hulley et al., 2018). These products have spatial and temporal resolutions of 1 km and 8 days, respectively."
>
> "Valid MxD21A2 pixels whose centers fell within the identified PV facility boundaries were retained and assigned to the nearest WRF PV grid cell. Within each 8-day period, the MODIS pixels assigned to the same WRF grid cell were averaged to obtain a grid-cell-scale MODIS LST value. The corresponding MOD21A1D and MYD21A1D daily products were used to identify the valid observation dates and satellite overpass times within each 8-day period. WRF TSK was linearly interpolated to these overpass times and then averaged over the same 8-day period for comparison with the MODIS observations."

Location: Sections 3.1 and 4.1.3, lines 184–188, 282–288; Fig. 4.

Specific Point 18: *L150: MODIS derived LST also accompanies retrieved surface emissivities in two IR bands. Is the effective surface emissivity in the model simulations consistent with the one reported by MODIS? This could affect interpretation of the skin temperature.*

Response: Thank you for this important comment. The mean MODIS Emis_31/32 over the PV areas was approximately 0.96, compared with emissivities of approximately 0.92 in WRF_CTL and 0.89 in WRF_PV. The grid-cell emissivity in WRF_PV is derived by combining the PV panel emissivity (0.82) with the ground emissivity through the surface-weighting scheme. The adopted upper-surface value of 0.82 is based on measurements reported by Heusinger et al. (2020), with a similar value reported by Sun et al. (2017). Previous studies have also reported lower measured PV panel emissivities than satellite-retrieved emissivities over solar-farm pixels (Fan and Huang, 2021). By contrast, MODIS provides band-specific emissivities for individual thermal-infrared bands, whereas land-surface and climate models generally use a broadband or effective longwave emissivity. In addition, PV-induced changes in vegetation cover, soil moisture, and shaded-ground fractions may further affect satellite-pixel effective emissivity (Hulley et al., 2010; Neinavaz et al., 2020; Wu et al., 2022). Similar model–satellite emissivity differences have been reported previously (Wang et al., 2014; Coll et al., 2024). Future work would benefit from additional field measurements of emissivity at PV sites to better constrain the model parameterization.

Specific Point 19: *Section 3.2: What is the temporal frequency and spatial resolution of these three datasets? If the spatial resolution is incompatible with the model grid, how are they incorporated into the model? Are these datasets consistent with each other so that at the transition points they do not introduce discontinuity issues? Specifically, the second and the third datasets have overlapping observations between 2019~2022. Do these two datasets agree? How many solar farms were selected as a result?*

Response: Thank you for this comment. We have revised Section 3.2 to clarify the temporal frequency and spatial form of the three PV datasets. The Photovoltaic Dataset of China covers 2013–2023 with a five-year temporal frequency and is provided as PV polygon vector data. We used its 2018 and 2023 layers. The Global Photovoltaic Solar Panel Dataset provides annual 20 m raster PV maps for 2019–2022. The China Photovoltaic Power Plant Vector Dataset provides the 2024 PV map as PV polygon vector data. Therefore, for the 2018–2024 simulations, each year was assigned only one prescribed PV distribution. There were no overlapping same-year PV maps from different datasets, including for 2019–2022.

We have also clarified how these PV maps were incorporated into WRF. The retained utility-scale PV areas were converted into a binary PV grid mask on the WRF D03 grid. A WRF grid cell was identified as a PV grid cell if it intersected with the retained PV polygons. This assignment provides a practical way to convert the PV data into a WRF grid-scale PV mask and avoids omitting utility-scale PV farms that straddle grid-cell boundaries. This treatment is consistent with the purpose of the present implementation, which is to introduce a physically based PV surface-energy scheme into WRF and represent the surface-energy response of PV-affected grid cells. To better represent PV installations, we are currently conducting research using deep learning methods to investigate PV effects at finer spatial scales.

To examine whether the use of different PV datasets introduced discontinuities at transition points, we added a year-to-year consistency check. For each adjacent-year transition, we separated retained, newly added, and lost PV areas. The total prescribed PV area increases monotonically from 205.68 km² in 2018 to 720.19 km² in 2024. After applying a 100 m spatial tolerance, the lost area accounted for only 0–2.56 % of the total PV area in each year. This small proportion indicates that the prescribed PV maps maintained strong spatial continuity across adjacent years and showed few artificial discontinuities. Finally, for the 2024 PV map, 40 utility-scale PV farms were selected.

The revised text reads:

> "Three datasets were used to characterize the spatial distribution of PV installations. The first was the Photovoltaic Dataset of China, which covers 2013–2023 at five-year intervals and is provided as PV polygon vector data (Lin, 2024). We used its 2018 and 2023 layers. The second was the Global Photovoltaic Solar Panel Dataset, which provides annual 20 m raster PV maps for 2019–2022 (Li et al., 2025a). The third was the China Photovoltaic Power Plant Vector Dataset, which provides the 2024 PV map as PV polygon vector data (Yang et al., 2025). All three datasets were based on high-resolution satellite imagery, generated using machine learning classification approaches, and validated against manually interpreted samples. For each simulation year, only one PV dataset was used to prescribe the PV distribution. To assess the spatial consistency across dataset transitions, the PV distributions in adjacent years were compared using a 100 m spatial tolerance. The lost area accounted for only 0–2.56 % of the total mapped PV area, indicating generally good spatial continuity across adjacent years. To align with the spatial resolution of the MODIS land surface temperature dataset, only PV facilities with areas greater than 1 km² were retained. The total mapped PV installation area increased from 205.68 km² in 2018 to 720.19 km² in 2024."

Location: Section 3.2, lines 190–203.

Specific Point 20: *L170: Please specify the exact values of the pressure levels.*

Response: Thank you for this comment. We apologize for the unclear wording. The 38 vertical levels used in the WRF simulations are not fixed pressure levels. WRF employs a terrain-following hybrid sigma–pressure vertical coordinate, and the pressure at the interior model levels varies spatially and temporally. In our configuration, the model used 38 vertical model levels, and the model-top pressure was set to 50 hPa.

Specific Point 21: *L179: "sea surface temperature [...] updated daily in the WRF simulations". Please confirm, as ERA5 provides hourly fields of sea surface temperature.*

Response: Thank you for pointing this out. We have confirmed that sea surface temperature was updated daily in our WRF simulations using ERA5 SST data at a 24 h interval.

Specific Point 22: *L182: "annual evolution of PV distribution" is a bit confusing. Is the fractional PV assigned every day that gradually grows with the installation of new solar farms? Or is the PV distribution constant in the simulated period of each year?*

Response: Thank you for pointing this out. We have clarified that the PV distribution was updated on an annual basis, not on a daily basis. For each simulation year, WRF_PV used the corresponding annual PV map, which was kept fixed throughout the summer simulation period. This treatment is consistent with the annual temporal resolution of the available PV datasets.

The revised text reads:

> "The first experiment (WRF_PV) incorporated a year-specific PV distribution, while the second experiment (WRF_CTL) used the original land-use data without PV installations. WRF_PV and WRF_CTL used identical initial and lateral boundary conditions and the same physical parameterization configuration described in Section 3.3. For each simulation year, the corresponding annual PV map was kept fixed throughout the simulation period in WRF_PV, consistent with the annual temporal resolution of the available PV datasets."

Location: Section 3.4, lines 228–232.

Specific Point 23: *L186: Is there any reason why this study focuses on the boreal summer seasons rather than including the boreal winter seasons?*

Response: Thank you for this helpful comment. We have revised the manuscript to clarify why boreal summer was selected. Summer was chosen because solar radiation is generally strong during this period, making it suitable for examining PV-induced radiative perturbations and surface energy responses. Moreover, land–atmosphere interactions are more active in summer and play an important role in East Asian summer climate variability (Zhang et al., 2011). In the study area, summer is the main season for water vapor transport and precipitation, accounting for approximately 62 % of the annual total precipitation (Zhang et al., 2023). Therefore, summer provides a useful period for demonstrating the capability of WRF-PV to represent PV-induced surface-energy and land–atmosphere responses.

We agree that winter and spring simulations are also important. However, extending the simulations to winter and spring would require additional seasonal processes that are not represented in the current WRF-PV framework. These include snow accumulation and shedding from PV panels in winter and dust deposition on panel surfaces in spring, both of which can affect PV power output and panel energy balance (Marion et al., 2013; Jiang et al., 2011). Including these season-specific processes is beyond the scope of the present model-demonstration study. We have clarified this limitation in the revised manuscript and noted that year-round simulations will be needed in future work to assess the seasonal dependence of PV–climate interactions.

The revised text reads:

> "Two sets of WRF simulations were conducted to assess the climatic response to utility-scale PV installations during summer, when solar radiation is strong and land–atmosphere coupling has been shown to play an important role in East Asian climate (Zhang et al., 2011)."
> "In addition, the simulations were limited to boreal summer. Winter applications would require explicit treatment of PV-specific snow accumulation, shedding, and removal, which can affect panel energy balance and power output."

Location: Sections 3.4 and 5, lines 226–228, 497–499.

Specific Point 24: *Section 3.4: How many ensemble member runs are conducted in this study? How would internal variability affect the results?*

Response: Thank you for this important comment. No multi-member ensemble simulations were conducted in this study. The experiments were designed as paired single-member sensitivity simulations for each year. For each summer from 2018 to 2024, WRF-PV and WRF-CTL were driven by the same initial conditions, lateral boundary conditions, and physical parameterization settings.

Therefore, the WRF-PV minus WRF-CTL difference for each year represents the PV-induced response under the same large-scale meteorological background.

The PV-induced response was averaged across the seven summers. This multi-year averaging helps reduce the influence of year-specific fluctuations and internal variability. In addition, t-tests were applied to the WRF-PV minus WRF-CTL differences in Sections 4.2 and 4.3 to examine whether the simulated mean responses are statistically distinguishable from zero.

The revised text reads:

> "At each hour of the diurnal cycle, the WRF_PV minus WRF_CTL difference from each day was treated as one sample, and a t-test was used to determine whether the mean difference was significantly different from zero."

Location: Section 4.2, lines 323–325.

Specific Point 25: *Figure 1: What is the total area of solar panel region?*

Response: Thank you for this suggestion. We have added the total mapped area of the solar panel. The total mapped PV installation area increased from 205.68 km² in 2018 to 720.19 km² in 2024.

The revised text reads:

> "The total mapped PV installation area increased from 205.68 km² in 2018 to 720.19 km² in 2024."

Location: Section 3.2, lines 202–203.

Specific Point 26: *Figures 2 and 3: please add bias maps (model – CMFD) since the spatial pattern panels alone do not show where the errors lie.*

> **Response:** Thank you for this suggestion. We have replaced CMFD with the higher-resolution CLDAS dataset at a spatial resolution of 0.0625° for model evaluation. We have added model – reanalysis bias maps to the revised figures to show the spatial distribution of model errors more clearly (Fig. R1.4, R1.5).

Location: Sections 4.1.1 and 4.1.2; Figs. 2–3.

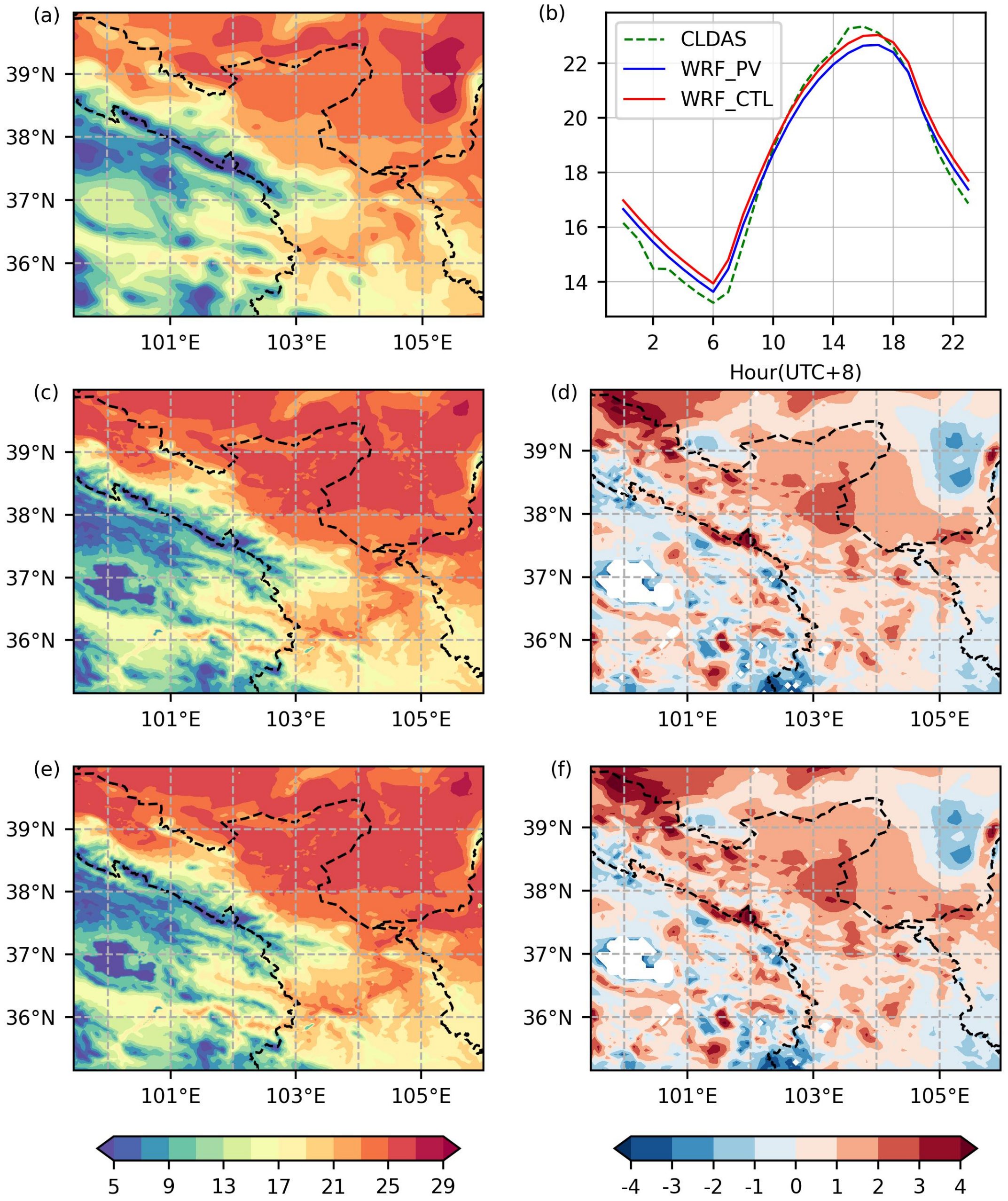

Figure R1.4: Spatial distribution of mean air temperature at 2 m height (T2, °C) during summer (June, July and August) in D03: (a) CLDAS, (c) WRF_PV, and (e) WRF_CTL; differences of (d) WRF_PV − CLDAS and (f) WRF_CTL − CLDAS. (b) Diurnal cycle of T2 averaged over the study area. (Figure 2 in the revised manuscript)

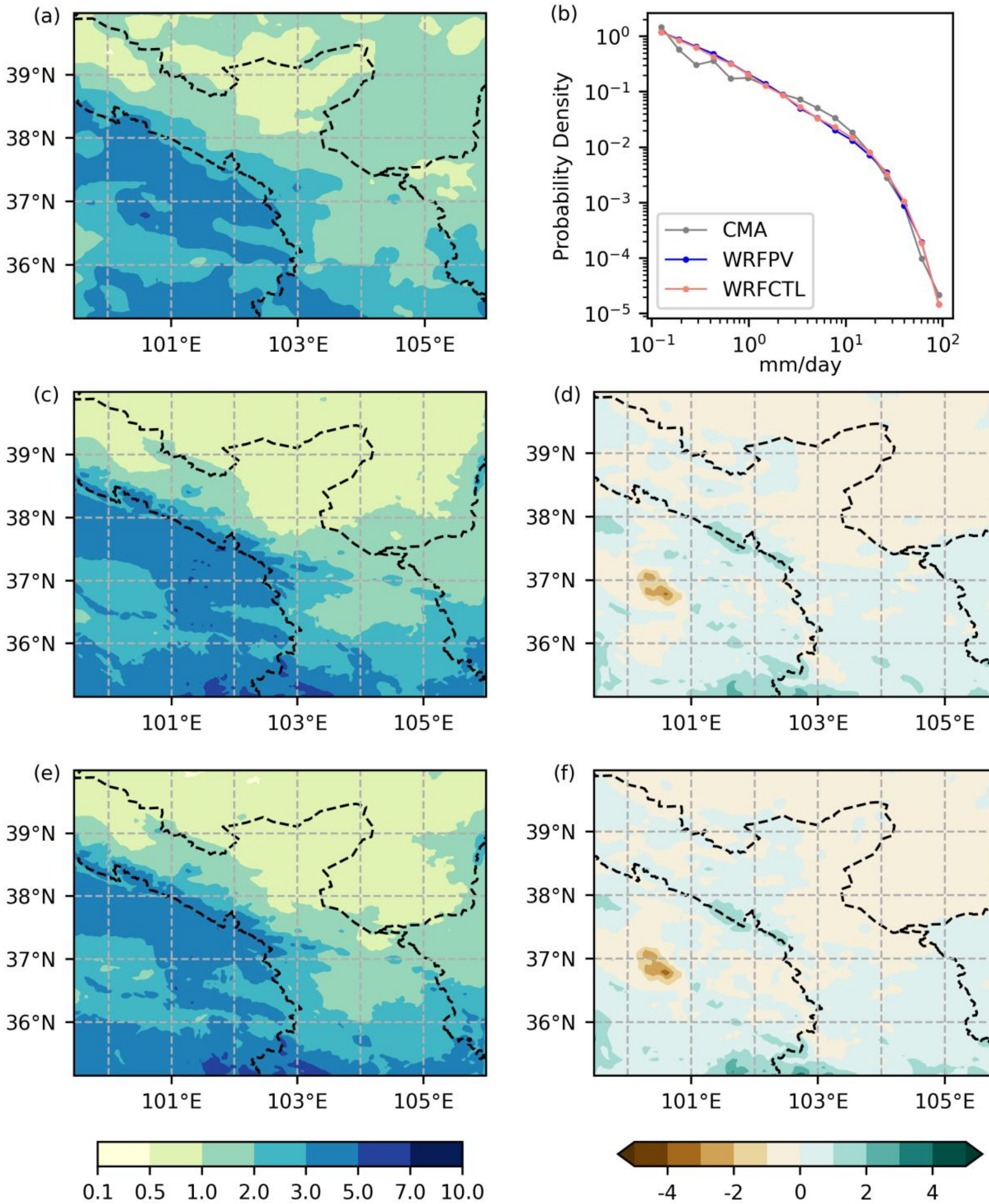

Figure R1.5: Spatial distribution of mean precipitation (mm day^{-1}) during summer in D03: (a) CLDAS, (c) WRF_PV, and (e) WRF_CTL; differences of (d) WRF_PV − CLDAS and (f) WRF_CTL − CLDAS. (b) Probability distribution of daily precipitation intensity derived from CMA station observations (grey line) and from WRF_PV (blue line) and WRF_CTL (red line). Simulation results were interpolated to station points. (Figure 3 in the revised manuscript)

Specific Point 27: *L197: Figure 4 is introduced before Figure 3.*

Response: Thank you for pointing this out. The original Figure 4 (Taylor diagram) has been removed, and the model performance is now quantified using bias and RMSE in the text.

Specific Point 28: *L225: How many valid MODIS samples are used in the analysis?*

Response: Thank you for this comment. A total of 10,310 valid 8-day MODIS–WRF collocations at the WRF grid-cell scale were retained. After spatial averaging within the corresponding WRF grid cells, 77 valid MODIS–WRF collocated samples were used in the analysis.

The revised text reads:

> "A total of 10,310 valid 8-day MODIS–WRF collocations were retained and used to construct the error distributions shown in Fig. 4. At each observation time, MODIS LST and WRF TSK were first averaged over all valid PV grid cells. Bias and RMSE were then calculated from the 77 paired time-mean samples."

Location: Section 4.1.3, lines 288–291; Fig. 4.

Specific Point 29: *L229: What is the mean bias value of both simulations? Given the large RMSE of over 3 K in both simulations, it is hard to argue that WRF_PV showed improved skills over the control simulation. What's the difference of RMSE over surrounding non-PV grid cells (to see whether the improvement is local to PV pixels).*

Response: Thank you for this valuable comment. In response to your suggestion, we refined the physical parameterization configuration and repeated the simulations. We have also added the mean bias values and calculated the evaluation statistics by first averaging TSK over all panel grid cells at each MODIS observation time and then calculating the statistics across the 77 observation times. WRF_CTL showed a mean bias of +0.697 K and an RMSE of 3.071 K, whereas WRF_PV showed a mean bias of −0.340 K and an RMSE of 2.560 K. WRF_PV therefore reduced the RMSE by 0.511 K relative to WRF_CTL.

Over the surrounding non-PV grid cells, RMSE decreased from 2.851 to 2.526 K in the first grid-cell ring and from 2.791 to 2.622 K in the 2–3-grid-cell ring. Thus, the improvement was strongest over the PV pixels and became weaker in the surrounding areas. These results have been added to the revised manuscript.

The revised text reads:

> "WRF_CTL produced a mean bias of +0.697 °C and an RMSE of 3.071 °C, whereas WRF_PV produced a mean bias of −0.340 °C and an RMSE of 2.560 °C. Thus, WRF_PV reduced the RMSE by 0.511 °C and reduced the magnitude of the mean bias relative to WRF_CTL. These results indicate that WRF_PV achieved better agreement with MODIS than WRF_CTL over the PV installations. We also evaluated TSK over the surrounding non-PV grid cells. In the first grid-cell ring surrounding the PV grid cells, the RMSE decreased from 2.851 °C in WRF_CTL to 2.526 °C in WRF_PV. In the second and third grid-cell rings, it decreased from 2.791 °C to 2.622 °C. Therefore, the RMSE reduction weakened with distance from the PV grid cells. Together, these results indicate that the improvement in WRF_PV was concentrated mainly over the PV installations."

Location: Section 4.1.3, lines 292–299; Fig. 4.

Specific Point 30: *Figure 5: x-axis label and unit are missing. What does the blue vertical line mean?*

Response: Thank you for pointing this out. In the revised manuscript, the former Figure 5 has been renumbered as Figure 4. We have added the x-axis label and unit, and clarified that the vertical dashed line denotes zero TSK error (WRF − MODIS = 0 °C) (Fig. R1.3).

***Specific Point 31:** Section 4.3: How are these local energy budget perturbations translated to the regional mean values (e.g., within the D3 domain)? This could partly answer the question of how large the radiative forcing of solar farms could impose on the regional climate system.*

Response: Thank you for this important comment. We estimated the regional-scale magnitude of the PV-induced surface radiative perturbation by weighting the simulated perturbation by the mean fractional area of PV grid cells within D03 during 2018–2024. The PV grid cells accounted for approximately 0.464 % of the D03 grid-cell area on average. The estimated daytime mean perturbations in net radiation and sensible heat flux over D03 were approximately +0.27 and +0.23 W m^{-2}, respectively.

The revised text reads:

> "To estimate the regional-scale magnitude of the PV-induced surface-energy perturbation, the local flux differences over the PV grid cells were weighted by the mean fractional area of PV grid cells within D03 during 2018–2024. The PV grid cells accounted for approximately 0.464 % of the D03 grid-cell area on average. This scaling yielded estimated daytime mean D03-averaged perturbations of approximately +0.27 W m^{-2} in net radiation and +0.23 W m^{-2} in sensible heat flux. These regional-mean perturbations were substantially smaller than the corresponding local changes over the PV grid cells because PV installations occupied only a small fraction of D03."

Location: Section 4.3, lines 382–387.

***Specific Point 32:** Section 4.3: It would strengthen the model-evaluation case to present a closed energy-balance budget table or schematic diagram (NetRad, SH, LH, GRDFLX, P_out — daytime mean, nighttime mean, 24 h mean) for both runs and verify closure to within a stated tolerance.*

Response: Thank you for this important suggestion. In the revised manuscript, we added a closed energy-budget table in Section 4.3. Table R1.3 reports net radiation, sensible heat flux, latent heat flux, ground heat flux, PV power output, the sum of the major energy-budget terms, and the residual term for both WRF-CTL and WRF-PV. Daytime is defined as 08:00–19:00 UTC+8, and nighttime is defined as 20:00–07:00 UTC+8. The residual is calculated as:

$$\text{Residual} = \text{NetRad} - (\text{SH} + \text{LH} + \text{GRDFLX} + \text{Pout}).$$

The revised text reads:

> "Table 2 summarizes the daytime, nighttime, and 24 h mean surface energy budgets over the WRF PV grid cells. The energy balance residual was calculated as the difference between net radiation and the sum of sensible heat flux, latent heat flux, ground heat flux, and electrical power output. In WRF_CTL, the residuals were −5.35, 0.06, and −2.64 W m^{-2} during daytime, nighttime, and over the full diurnal cycle, respectively. The corresponding residuals in WRF_PV were 2.92, 4.73, and 3.83 W m^{-2}. This result indicates that the implemented PV–ground energy-balance scheme maintained approximate numerical energy closure."

Location: Section 4.3, lines 372–377; Table 2.

Table R1.3: Daytime, nighttime, and 24 h mean surface energy budget components over the WRF PV grid cells. All values are in W m^{-2}. (Table 2 in the revised manuscript)

Period	Experiment	NetRad	SH	LH	GRDFLX	Pout	Sum of terms	Residual
Daytime	WRF-CTL	282.70	164.58	43.01	80.46	0.00	288.05	−5.35
Daytime	WRF-PV	341.05	214.55	36.86	64.05	22.67	338.13	2.92
Nighttime	WRF-CTL	−66.58	−3.88	5.85	−68.60	0.00	−66.63	0.06
Nighttime	WRF-PV	−63.18	−20.30	5.63	−53.41	0.16	−67.91	4.73
24 h mean	WRF-CTL	108.06	80.35	24.43	5.93	0.00	110.71	−2.64
24 h mean	WRF-PV	138.93	97.13	21.24	5.32	11.41	135.11	3.83

Specific Point 33: *L268: "specular reflection from the PV panels at large solar zenith angles". Is the angular dependence of panel albedo parameterized? I suspect this is in fact a numerical artifact of Eq. (2) with a constant panel albedo value.*

Response: Thank you for this important comment. The albedo of the front PV surface is calculated from the Fresnel law as an angle-dependent reflectance. Therefore, the enhanced reflected shortwave radiation at large solar zenith angles is not a numerical artifact, but results from the angle-dependent reflectance of the PV front surface. We have clarified this treatment in the model-description section.

The revised text reads:

> "$\alpha_{PV,top}$ denotes the albedo of the front PV surface, calculated from the Fresnel law as an angle-dependent reflectance."

Location: Sections 2.1 and 4.3, lines 112–113.

Specific Point 34: *Figure 8: The figure does not have multiple panels, yet the caption includes "(a)".*

Response: Thank you for pointing this out. In the revised manuscript, the former Figure 8 has been renumbered as Figure 7. We have removed "(a)" from the caption of Figure 7.

Specific Point 35: *L316: additional comma at the end of the sentence.*

Response: Thank you for noting this. We have removed the additional comma at the end of the sentence.

Specific Point 36: *Figure 9: The SW_down decrease is attributed to "an increase in low cloud fraction" (L308~309) and Fig. 9 shows positive low-cloud anomaly as well as increasing updraft. It is also possible that increased atmospheric water vapour absorption from the enhanced surface-air mixing could also contribute. I suggest at least adding a decomposition of the SW_down anomaly into clear-sky and cloud components and, optionally, quantify the change in column-integrated water vapour and aerosol optical depth.*

Response: Thank you for this helpful suggestion. In the revised manuscript, the former Figure 9 has been renumbered as Figure 8. A clear-sky and cloud decomposition of the SWdown anomaly is not available from the existing simulations because the Dudhia shortwave radiation scheme does not diagnose clear-sky downward shortwave radiation.

To assess the possible contribution of atmospheric water vapour, we quantified the change in column-integrated water vapour between WRF_PV and WRF_CTL. The WRF_PV minus WRF_CTL difference is approximately −0.2 kg m^{-2}, corresponding to a decrease of about 1 %. This indicates that water vapour absorption was not the primary cause of the simulated reduction in SWdown.

Aerosol was not directly simulated in the current model setup, and the Dudhia scheme used the same prescribed clear-sky scattering parameter in both experiments. Overall, the increased cloud fraction, together with enhanced upward motion and reduced lower-atmospheric stability, indicates that enhanced cloud attenuation was the primary contributor to the reduction in SWdown.

The revised text reads:

> "In contrast, column-integrated water vapor decreased by approximately 0.2 kg m^{-2} (about 1 %) in WRF_PV relative to WRF_CTL, indicating that water vapor absorption was unlikely to be the primary cause of the SWdown reduction."

Location: Section 4.3, lines 394–396; Fig. 8.

***Specific Point 37:** Figure 10: Explain the elements of the box plot. What is the red curve? Also it is important to note that all differences are statistically insignificant. Maybe examine the spatial pattern of the extreme- precipitation change so that we can see whether it is correlated with PV location, downstream of it, or essentially noise?*

Response: Thank you for this helpful suggestion. We have removed the original Figure 10, including the box plot and the red curve. We replaced it with two spatially explicit figures to examine the precipitation changes and their associated atmospheric conditions more directly.

Figure R1.6 presents the spatial differences in mean precipitation and cumulative extreme precipitation (>30 mm day^{-1}, following the definition of CMA) between WRF_PV and WRF_CTL, together with the probability distributions of daily precipitation. Although the domain-mean precipitation difference was small, the spatial response was pronounced. Precipitation generally increased over the central and southern parts of the domain and decreased over several northern and western areas. Accumulated extreme precipitation showed a more localized spatial response than mean precipitation. WRF_PV also showed a slightly higher probability density for heavy rainfall of 60–100 mm day^{-1}, suggesting a modest shift toward more intense rainfall events.

Figure R1.7 illustrates the atmospheric conditions associated with these spatial changes, including terrain, background winds, sensible heat flux, low-level wind perturbations, vertical motion, and vertically integrated water vapor flux divergence. We take the extreme-precipitation increase near 38.6° N as an example because this area is located well within the model domain and is largely free from lateral boundary effects. Enhanced upward motion and moisture convergence occurred over the main areas of increased precipitation. Increases in sensible heat flux over the PV clusters were accompanied by convergence perturbations in the low-level wind field. The easterly, southeasterly, and northeasterly wind anomalies flowed toward the PV clusters and ascended along the mountain range marking the northern boundary of Gansu Province, inducing weak upward motion. Although the anomalous ascent produced only a small change in mean precipitation, it could enhance extreme precipitation under favorable conditions. The spatial correspondence among sensible heating, circulation perturbations, vertical motion, moisture convergence, and precipitation provides a dynamically coherent interpretation of the extreme-precipitation response.

The revised text reads:

> "Figure 9 shows the spatial distributions of the changes in daily mean and cumulative extreme precipitation between WRF_PV and WRF_CTL together with the probability density distributions of daily precipitation. The domain-mean precipitation difference between WRF_PV and WRF_CTL was small, indicating little change in the overall summer precipitation amount (Fig. 9a). However, the spatial response was pronounced, with precipitation increasing mainly over the central and southern parts of the domain and decreasing over several northern and western areas. Despite only small changes in mean precipitation (Fig. 9a), the related changes in water vapor convergence, vertical motion, and precipitation were dynamically coherent (Fig. 10c and 10d). This precipitation response pattern was broadly consistent with the period difference in the reanalysis data (Fig. S1). Accumulated extreme precipitation showed a more distinct and localized spatial response than mean precipitation (Fig. 9b). The probability distributions of WRF_PV and WRF_CTL were generally similar for light and moderate rainfall. However, WRF_PV showed a slightly higher probability density for heavy rainfall of 60–100 mm day^{-1}, suggesting a modest shift toward more intense rainfall events (Fig. 9c). A broadly similar shift in the daily precipitation distribution was also evident between the two periods in the reference dataset (Fig. S2)."
>
> "In order to understand the association of the changes in circulation and precipitation with the PV distribution, Figures 10a and 10b show the summer-mean low-level circulation and the change in sensible heat caused by PV deployment. The climatological low-level flow was predominantly southeasterly and closely influenced by the regional topography (Fig. 10a). The climatological precipitation field exhibited pronounced spatial heterogeneity, with higher precipitation over the plateau, where the low-level flow encountered rising terrain (Fig. 3a and 10a). Between 36° and 37° N, PV-induced sensible heating strengthened low-level convergence, accompanied by an enhanced easterly flow and water vapor transport toward the plateau (Fig. 10b). This circulation anomaly reinforced the existing terrain-related convergence and ascent (Fig. 10c and 10d), contributing to increased precipitation over northern Qinghai. Moreover, we take the area of extreme precipitation near 38.6° N, which is located well within the model domain and is largely free from lateral boundary effects, as an example (Fig. 9b). Increases in sensible heat flux were concentrated over the PV clusters and were accompanied by convergence in the low-level wind field (Fig. 10b). The easterly, southeasterly, and northeasterly wind anomalies flowed toward the PV clusters and ascended along the mountain range that marks the northern boundary of Gansu Province (Fig. 10a), inducing weak upward motion (Fig. 10c). Although this weak anomalous ascent led to only a slight modification of mean precipitation (Fig. 9a), it could produce enhanced extreme precipitation under appropriate conditions (Fig. 9b). These spatial correspondences suggested that PV-induced increases in sensible heat flux perturbed the local circulation, while the background flow and complex terrain modulated the locations of the resulting ascent, moisture convergence, and precipitation enhancement."

Location: Section 4.4, lines 409–441; Figs. 9–10.

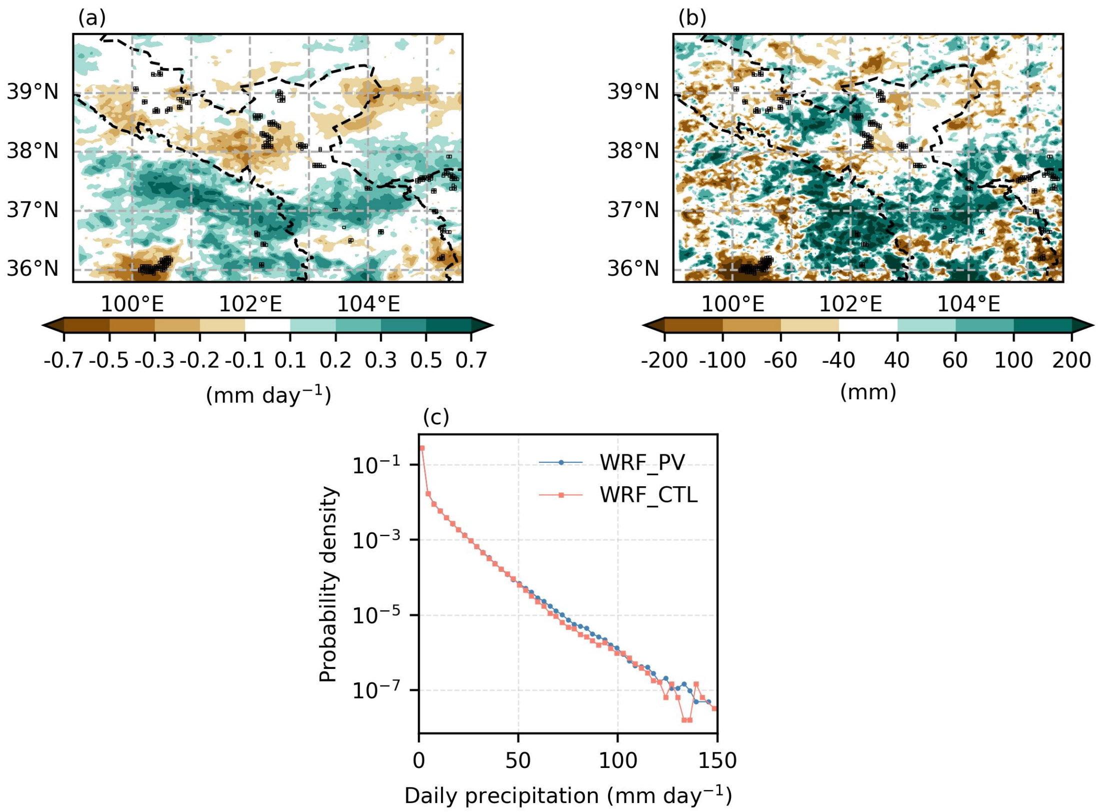

Figure R1.6: Spatial changes and probability density distributions of summer precipitation during 2018–2024. (a) Difference in mean daily precipitation between WRF_PV and WRF_CTL. (b) Difference in cumulative extreme precipitation (>30 mm day^{-1}) amount between WRF_PV and WRF_CTL. (c) Probability density distributions of daily precipitation intensity in WRF_PV and WRF_CTL over D03. In (a) and (b), grey grid symbols denote PV grid cells. (Figure 9 in the revised manuscript)

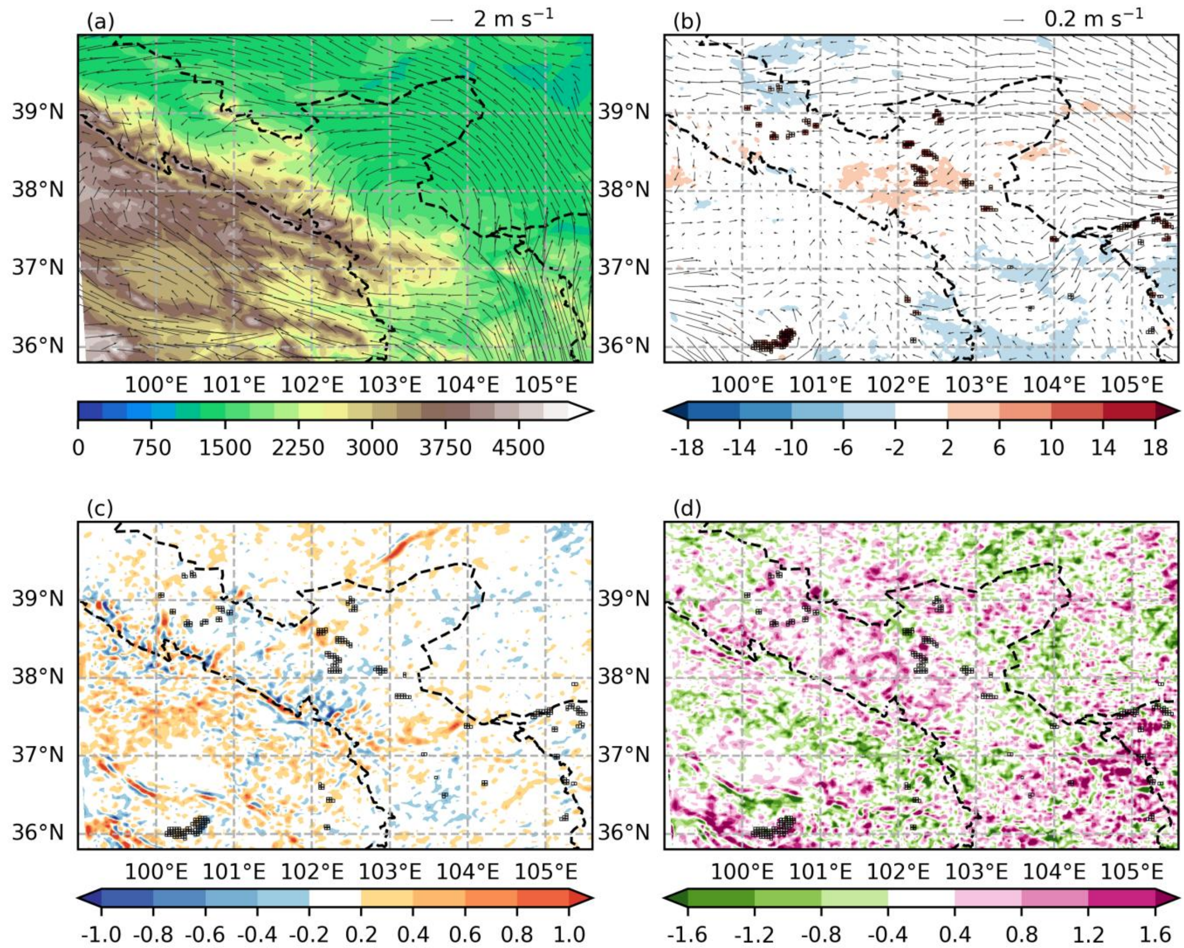

Figure R1.7: Terrain and atmospheric processes during the summers of 2018–2024. (a) Terrain height (m, shading) and near-surface wind field in WRF_CTL (vectors). (b) Differences in sensible heat flux (W m^{-2}, shading) and near-surface wind field (vectors). (c) Difference in vertical velocity (cm s^{-1}), with positive values indicating enhanced upward motion. (d) Difference in vertically integrated water vapor flux divergence (10^{-5} kg m^{-2} s^{-1}), with negative values indicating enhanced moisture convergence. All differences are calculated as WRF_PV minus WRF_CTL. In (b–d), grey grid symbols denote PV grid cells. (Figure 10 in the revised manuscript)

Specific Point 38: *L355~366: Related to General Suggestion #1, the conclusion makes a reasonable case that the present model produces smaller anomalies than the effective-albedo Sahara studies because of correct treatment of inter-row ground and panel thermal capacity. It would be even better to demonstrate this directly: i.e., run a third experiment in which the WRF-PV scheme is replaced by an effective-albedo formulation in the same domain, and show that the over-estimation reproduces.*

Response: Thank you for this constructive suggestion. Following the reviewer's recommendation, we conducted an additional experiment, WRF_EA, in which the physically based WRF-PV scheme was replaced by the effective albedo formulation following Li et al. (2018). WRF_EA retained the same domain, simulation period, and physical configuration as WRF_PV and WRF_CTL, and used the same PV spatial distribution as WRF_PV. A constant effective albedo of 0.15 was prescribed for all PV grid cells. Details of the experimental design, effective albedo formulation, and evaluation results have been added to Supplementary Text S2 and Table S1.

The new experiment reproduced the overestimation most clearly in skin temperature and precipitation. WRF_EA produced a mean TSK bias of +2.62 °C and an RMSE of 4.02 °C, both larger than those of WRF_PV (−0.34 and 2.56 °C) and WRF_CTL (+0.70 and 3.07 °C). Its precipitation bias and RMSE were +0.14 and 1.06 mm day^{-1}, respectively, compared with WRF_PV (+0.08 and 0.55 mm day^{-1}) and WRF_CTL (+0.05 and 0.55 mm day^{-1}) (Table R1.1). Relative to WRF_CTL, WRF_EA and WRF_PV produced contrasting TSK responses. WRF_EA increased TSK, whereas WRF_PV produced daytime TSK cooling, which is more consistent with the daytime surface cooling reported in previous satellite-based studies. The domain-scale T2 bias was comparable among the three experiments, although the T2 RMSE was larger in WRF_EA. We therefore do not interpret the effective albedo method as producing a uniformly stronger response across all variables. These results highlight the limitations of representing PV installations solely through bulk albedo. We have therefore revised the discussion to focus on the directly supported differences in TSK and precipitation, together with the limitations of the EA representation.

The revised text reads:

> "To compare WRF-PV with the effective albedo (EA) method of Li et al. (2018), we conducted an additional experiment (WRF_EA) in which the WRF-PV scheme was replaced by the EA method. The model domain, simulation period, and physical configuration remained unchanged. Details of the experimental design and the complete evaluation results are provided in Supplementary Text S2. WRF_EA produced a mean TSK bias of +2.62 °C and an RMSE of 4.02 °C, both larger than those of WRF_PV (−0.34 and 2.56 °C) and WRF_CTL (+0.70 and 3.07 °C). Relative to WRF_CTL, WRF_EA increased TSK, whereas WRF_PV produced daytime surface cooling. The warming simulated by WRF_EA contrasts with the daytime cooling reported by previous satellite-based studies of utility-scale PV farms (Zhang and Xu, 2020; Fan and Huang, 2021; Li et al., 2021; Wang et al., 2024; Xu et al., 2024). These contrasting responses highlight the limitations of representing PV installations solely through the bulk albedo of the entire grid cell. The EA method does not account for shading and the associated changes in ground heat storage. By contrast, WRF-PV explicitly represented panel coverage, panel thermal properties, and shading effects, and showed closer agreement with MODIS."

Location: Section 5, lines 470–480; Supplementary Text S2 and Table S1.

Specific Point 39: *L367: "this study considered only the evaporation change". I assume the authors mean that this study only analyzes the latent heat and precipitation variables, not that soil moisture was held fixed, is that correct?*

Response: Thank you for pointing out this ambiguity. Yes, your interpretation is correct. We did not mean that soil moisture was held fixed in the simulations. Soil moisture evolved interactively within the Noah land-surface model in both WRF_CTL and WRF_PV. The intended meaning was that this study mainly analyzed latent heat flux responses, but did not systematically diagnose soil moisture changes or vegetation-related feedbacks. We have revised the sentence to avoid this misunderstanding. The revised text now clarifies that soil moisture was not prescribed or fixed.

The revised text reads:

> "The present analysis focused on surface energy balance and land–atmosphere responses. Although soil moisture evolved interactively in the Noah land-surface model, its response to PV-induced shading was not systematically diagnosed."

Location: Section 5, lines 500–501.

Specific Point 40: *Section 5: The discussion of the implications from this study seems thin. Some ideas: how easily WRF-PV can be ported to other land-surface schemes and at what computational cost; what evaluation data would most help future development; how the SW_down feedback (−1%) translates into a reduction in power production.*

Response: Thank you for this helpful suggestion. We have expanded Section 5 to discuss the portability, computational cost, evaluation needs, and power-production implications of the model. We clarified that the model can, in principle, be coupled with other land-surface schemes through interface adaptation, and a one-day benchmark showed only a 0.7 % increase in runtime relative to WRF_CTL. We also identified broader field measurements of module and near-surface air temperatures, surface energy fluxes, and power output as priorities for future evaluation. In addition, the simulated 1.2 % reduction in SWdown implies that PV-induced atmospheric feedbacks may affect the local solar resource, with implications for PV yield estimation.

The revised text reads:

> "Additionally, PV-induced atmospheric feedbacks reduced SWdown by approximately 1.2 %, affecting the local solar resource, with implications for PV yield estimation."
>
> "WRF-PV can, in principle, be coupled with other land-surface schemes because the PV module is implemented outside the land-surface model subroutine. Such applications would mainly require adapting the input–output interface and the treatment of ground temperature beneath the panels. A one-day wall-clock benchmark showed that WRF-PV increased the model runtime by only 0.7 % relative to WRF_CTL."
>
> "Future evaluation would benefit from broader field observations of module and near-surface air temperatures, surface energy fluxes, and power output to better constrain the energy partitioning represented by WRF-PV."

Location: Section 5, lines 467–468, 481–484, 491–492.

Response to Reviewer 2

The study develops a fully coupled PV–climate model that captures energy balance and atmospheric feedbacks. Applied to northwestern China, it improves skin-temperature simulation and shows that PV cools the surface but warms the near-surface air in summer. PV increases sensible heating, reduces stability, enhances low clouds, lowers shortwave radiation, and shifts precipitation toward more extremes. The authors highlight the need for coupled PV–land–atmosphere modeling to assess climate impacts. The manuscript is well-written, but I have some concerns:

Response: We sincerely thank you for your valuable comments and constructive suggestions. We have substantially revised the manuscript to address all the concerns raised in the review. First, we strengthened the evaluation and mechanistic analysis of the simulated cloud and precipitation responses. Second, we clarified the treatment of the annual PV datasets and the paired experimental design, and further evaluated the radiative parameterization and surface energy balance closure. Third, we clarified the distinction between WRF-PV and previous modeling approaches by conducting an additional effective albedo experiment and directly comparing the different implementations. Fourth, we expanded the discussion of ecosystem processes and their implications for future model development. In addition, we updated the WRF physical configuration and adopted the higher-resolution CLDAS dataset. We then repeated the simulations and diagnostic analyses and redrew the figures. Detailed responses to each of these concerns are provided below.

Comment 1: *Line 155: A major concern is the consistency and potential bias introduced by merging multiple PV datasets with different temporal coverages (2013–2023 vs. 2019–2022 vs. 2024) and classification methodologies. The manuscript does not clearly explain how discrepancies among these sources (e.g., spatial overlap, differing detection accuracies, or temporal mismatches) were reconciled into a unified PV distribution. In addition, filtering out installations smaller than 1 km² to match MODIS resolution may systematically exclude a large fraction of PV capacity, potentially biasing the spatial representation and subsequent analysis. The authors may clarify the data harmonization process and assess how these choices affect the robustness of their results.*

Response: Thank you for this comment. We have revised Section 3.2 to clarify the temporal coverage and spatial formats of the three PV datasets, the selection of the annual PV maps, and the spatial consistency across dataset transitions. The Photovoltaic Dataset of China covers 2013–2023 with a five-year temporal frequency and is provided as PV polygon vector data. We used its 2018 and 2023 layers. The Global Photovoltaic Solar Panel Dataset provides annual 20 m raster PV maps for 2019–2022. The China Photovoltaic Power Plant Vector Dataset provides the 2024 PV map as PV polygon vector data. Therefore, for the 2018–2024 simulations, only one annual PV map was available for each simulation year, and no same-year fusion or treatment of cross-dataset spatial overlap was required. All three datasets were derived from high-resolution satellite imagery using machine-learning-based methods and validated against manually interpreted reference samples, providing a common basis for quality assurance.

We also assessed the spatial consistency across dataset transitions. After applying a 100 m spatial tolerance, the lost area accounted for only 0–2.56 % of the total PV area in each year. This small proportion indicates that the prescribed PV maps maintained strong spatial continuity across adjacent years and showed few artificial discontinuities.

Across the 2018–2024 PV maps, PV installations smaller than 1 km² accounted for no more than 7.5 % of the total PV area in any year, indicating that the filtering retained the dominant share of PV-covered area throughout the study period. To further address the exclusion of smaller PV installations, future simulations can be conducted at higher spatial resolutions with increased computational resources and higher-resolution PV datasets. In parallel, we are currently conducting deep-learning-based research to investigate PV effects under finer and more realistic spatial scenarios.

The revised text reads:

> "Three datasets were used to characterize the spatial distribution of PV installations. The first was the Photovoltaic Dataset of China, which covers 2013–2023 at five-year intervals and is provided as PV polygon vector data (Lin, 2024). We used its 2018 and 2023 layers. The second was the Global Photovoltaic Solar Panel Dataset, which provides annual 20 m raster PV maps for 2019–2022 (Li et al., 2025a). The third was the China Photovoltaic Power Plant Vector Dataset, which provides the 2024 PV map as PV polygon vector data (Yang et al., 2025). All three datasets were based on high-resolution satellite imagery, generated using machine learning classification approaches, and validated against manually interpreted samples. For each simulation year, only one PV dataset was used to prescribe the PV distribution. To assess the spatial consistency across dataset transitions, the PV distributions in adjacent years were compared using a 100 m spatial tolerance. The lost area accounted for only 0–2.56 % of the total mapped PV area, indicating generally good spatial continuity across adjacent years. To align with the spatial resolution of the MODIS land surface temperature dataset, only PV facilities with areas greater than 1 km² were retained. Across the 2018–2024 PV maps, PV installations smaller than 1 km² accounted for no more than 7.5 % of the total PV area in any year, indicating that the filtering retained the dominant share of PV-covered area throughout the study period. The total mapped PV installation area increased from 205.68 km² in 2018 to 720.19 km² in 2024."

Location: Section 3.2, lines 190–203.

Comment 2: *Line 180: While WRF_PV includes the "annual evolution" of PV distribution, it is still unclear whether WRF_CTL uses time-invariant land-use and how interannual variability is separated from PV-induced signals. Without a clear description of how PV changes are synchronized with the meteorological forcing and how differences are aggregated across years, the attribution of climate responses specifically to PV installations may be confounded. I suggest clarifying whether both experiments use identical atmospheric boundary conditions for each year, how PV expansion is implemented year by year, and whether sensitivity tests were performed to isolate PV effects from natural variability.*

Response: Thank you for this helpful comment. We have clarified the experimental design and aggregation procedure. WRF_PV and WRF_CTL were conducted as paired single-member sensitivity simulations for each summer from 2018 to 2024. The two experiments used identical meteorological initial and boundary conditions, physical parameterization schemes, and non-PV land-surface conditions. Thus, the two simulations differed only in the treatment of PV installations. In WRF_PV, PV expansion was represented through year-specific PV maps. For each year, the corresponding PV map was kept fixed throughout the summer simulation, consistent with the temporal resolution of the available datasets. In WRF_CTL, the original land-use field was held constant throughout 2018–2024, with no PV installations prescribed.

To isolate the PV-induced effects from natural variability, the analysis was based on the paired differences between WRF_PV and WRF_CTL. At each hour of the diurnal cycle, the difference from each day was treated as one sample, and a t-test was used to assess whether the mean difference was statistically significant.

The revised text reads:

> "Two sets of WRF simulations were conducted to assess the climatic response to utility-scale PV installations during summer, when solar radiation is strong and land–atmosphere coupling has been shown to play an important role in East Asian climate (Zhang et al., 2011). The first experiment (WRF_PV) incorporated a year-specific PV distribution, while the second experiment (WRF_CTL) used the original land-use data without PV installations. WRF_PV and WRF_CTL used identical initial and lateral boundary conditions and the same physical parameterization configuration described in Section 3.3. For each simulation year, the corresponding annual PV map was kept fixed throughout the simulation period in WRF_PV, consistent with the annual temporal resolution of the available PV datasets. The utility-scale PV areas were converted into a binary PV grid mask on the WRF D03 grid. A WRF grid cell was identified as a PV grid cell if it intersected with the PV area. In WRF_PV, the PV-ground coupling scheme updated surface temperature and energy fluxes at PV grid cells and enabled an explicit representation of PV-atmosphere feedback. Each simulation ran separately for the period of 2018–2024, with simulations initialized on 1 May and terminated on 31 August. The first month (May) was discarded as the model spin-up period, while the remaining three months (June–August) were used for analysis."

Location: Sections 3.4 and 4.2, lines 226–237, 323 – 325.

Comment 3: *Line 265: The authors attribute the large increase in net radiation primarily to reduced SWup and LWup, yet it is unclear whether these magnitudes are consistent with realistic PV albedo, emissivity, and panel orientation assumptions. In particular, the role of specular reflection and its parameterization in the model is not sufficiently described, raising questions about whether the shortwave radiative behavior of PV panels is accurately represented. It would be helpful if the authors provided a clearer description and validation of the radiative parameterization (including albedo, emissivity, and angular dependence) and demonstrated that surface energy balance closure is maintained under these large flux changes.*

Response: Thank you for this important comment. In WRF-PV, the front-surface reflectance is calculated from the Fresnel law as a function of the solar incidence angle, following Duffie and Beckman (2013). The incidence angle accounts for the solar zenith angle, solar azimuth angle, panel tilt, and panel azimuth. In the present simulations, the panels were represented as fixed-tilt arrays with a tilt angle of 37° and a south-facing azimuth of 0° based on an in situ observation (Jiang et al., 2021).

As an observational consistency check, we compared the simulated daytime albedo over the PV grid cells with available field observations. The daytime value decreased from approximately 0.224 in WRF_CTL to approximately 0.140 in WRF_PV. This is consistent with Ying et al. (2023), who reported mean broadband shortwave albedo values of 0.22 at a nearby Gobi Desert site and 0.14 at a PV site. The observed PV-site albedo was also higher in the early morning and late afternoon, consistent with the angle-dependent Fresnel formulation. For emissivity, the prescribed front- and rear -surface emissivities are 0.82 and 0.97, respectively, following the measurements of Heusinger et al. (2020). Sun et al. (2017) similarly reported an emissivity of approximately 0.82 for commercial solar glass.

In the revised manuscript, we added a closed energy-budget table in Section 4.3 for WRF_CTL and WRF_PV. The energy-balance residual was calculated as:

$$\text{Residual} = \text{NetRad} - (\text{SH} + \text{LH} + \text{GRDFLX} + \text{Pout}).$$

Table R2.1 shows that the residual remained small compared with the major energy fluxes. In WRF_CTL, the residuals were −5.35, 0.06, and −2.64 W m^{-2} during daytime, nighttime, and over the full diurnal cycle, respectively. The corresponding residuals in WRF_PV were 2.92, 4.73, and 3.83 W m^{-2}. This result indicates that the implemented PV–ground energy-balance scheme maintained approximate numerical energy closure.

Table R2.1: Daytime, nighttime, and 24 h mean surface energy budget components over the WRF PV grid cells. All values are in W m^{-2}. (Table 2 in the revised manuscript)

Period	Experiment	NetRad	SH	LH	GRDFLX	Pout	Sum of terms	Residual
Daytime	WRF-CTL	282.70	164.58	43.01	80.46	0.00	288.05	−5.35
Daytime	WRF-PV	341.05	214.55	36.86	64.05	22.67	338.13	2.92
Nighttime	WRF-CTL	−66.58	−3.88	5.85	−68.60	0.00	−66.63	0.06
Nighttime	WRF-PV	−63.18	−20.30	5.63	−53.41	0.16	−67.91	4.73
24 h mean	WRF-CTL	108.06	80.35	24.43	5.93	0.00	110.71	−2.64
24 h mean	WRF-PV	138.93	97.13	21.24	5.32	11.41	135.11	3.83

The revised text reads:

"$\alpha_{PV,top}$ denotes the albedo of the front PV surface, calculated from the Fresnel law as an angle-dependent reflectance. "

"Table 2 summarizes the daytime, nighttime, and 24 h mean surface energy budgets over the WRF PV grid cells. The energy balance residual was calculated as the difference between net radiation and the sum of sensible heat flux, latent heat flux, ground heat flux, and electrical power output. In WRF_CTL, the residuals were −5.35, 0.06, and −2.64 W m^{-2} during daytime, nighttime, and over the full diurnal cycle, respectively. The corresponding residuals in WRF_PV were 2.92, 4.73, and 3.83 W m^{-2}. This result indicates that the implemented PV–ground energy-balance scheme maintained approximate numerical energy closure."

Location: Sections 2.1 and 4.3, lines 112–113, 372–377; Tables 1 and 2.

***Comment 4:** Line 355: The discussion is not rigorously demonstrated. Other factors, such as differences in model configuration, domain size, resolution, boundary conditions, or background climate regimes, can also contribute to the discrepancy with previous studies. Without controlled sensitivity experiments (e.g., toggling only albedo treatment while keeping other processes identical), it is difficult to isolate which mechanisms drive the reduced magnitude of impacts, right? Some sensitivity tests should be considered. While the WRF-PV model is described as more physically realistic, the claim that it produces results "closer to observations" is not sufficiently justified, particularly for land-atmosphere interactions.*

Response: Thank you for this constructive suggestion. We agree that differences among previous studies may reflect multiple factors in addition to the PV representation. We therefore conducted a WRF_EA experiment replacing the physically based WRF-PV scheme with the effective albedo formulation of Li et al. (2018). All other model settings, simulation periods, meteorological forcing, and annual PV distributions were unchanged. The only difference was the representation of PV installations, with a constant effective albedo of 0.15 prescribed over the PV grid cells. WRF_EA produced a TSK bias of +2.62 °C and an RMSE of 4.02 °C relative to MODIS, both larger than those of WRF_PV and WRF_CTL, and it increased TSK relative to WRF_CTL, whereas WRF_PV produced daytime surface cooling. WRF_EA also yielded larger T2 and precipitation RMSEs. Further details are provided in Supplementary Text S2 and Table S1.

The revised text reads:

> "To compare WRF-PV with the effective albedo (EA) method of Li et al. (2018), we conducted an additional experiment (WRF_EA) in which the WRF-PV scheme was replaced by the EA method. The model domain, simulation period, and physical configuration remained unchanged. Details of the experimental design and the complete evaluation results are provided in Supplementary Text S2. WRF_EA produced a mean TSK bias of +2.62 °C and an RMSE of 4.02 °C, both larger than those of WRF_PV (−0.34 and 2.56 °C) and WRF_CTL (+0.70 and 3.07 °C). Relative to WRF_CTL, WRF_EA increased TSK, whereas WRF_PV produced daytime surface cooling. The warming simulated by WRF_EA contrasts with the daytime cooling reported by previous satellite-based studies of utility-scale PV farms (Zhang and Xu, 2020; Fan and Huang, 2021; Li et al., 2021; Wang et al., 2024; Xu et al., 2024). These contrasting responses highlight the limitations of representing PV installations solely through the bulk albedo of the entire grid cell. The EA method does not account for shading and the associated changes in ground heat storage. By contrast, WRF-PV explicitly represented panel coverage, panel thermal properties, and shading effects, and showed closer agreement with MODIS."

Location: Section 5, lines 470–480; Supplementary Text S2 and Table S1.

***Comment 5:** Line 355: Given that the study highlights differences in cloud fraction and precipitation characteristics (including extremes), more rigorous validation against observational or reanalysis datasets is needed. This is especially important because precipitation redistribution (rather than total change) is a central conclusion.*

Response: Thank you for this helpful comment. We replaced the original precipitation box plot with spatial analyses of summer mean precipitation and accumulated extreme precipitation, together with the daily precipitation distributions (Fig. R2.1). The revised results show little change in domain-mean precipitation but clear spatial heterogeneity, including localized changes in extreme precipitation. Both the spatial precipitation response and the shift in the daily precipitation distribution showed broad similarity to the corresponding interperiod changes in the reanalysis dataset (Figs. R2.2–R2.3). Although these changes also contain signals of long-term climate change, the observed similarities partly support the simulated PV-related precipitation redistribution. To investigate the mechanism underlying this redistribution, Fig. R2.4 illustrates the PV-induced changes in sensible heat flux, low-level convergence, moisture convergence, and vertical motion. These changes were spatially coherent with the precipitation response, suggesting that PV-induced sensible heating, together with terrain-related ascent, contributed to the localized precipitation enhancement. As the conclusion focuses on the reduction in downward shortwave radiation, we added a corresponding interperiod analysis using the reanalysis dataset. The later period also showed reduced downward shortwave radiation, consistent with the direction of the simulated radiative response. The low-cloud increase is therefore discussed as a model-diagnosed mechanism contributing to this radiative response (Table R2.2).

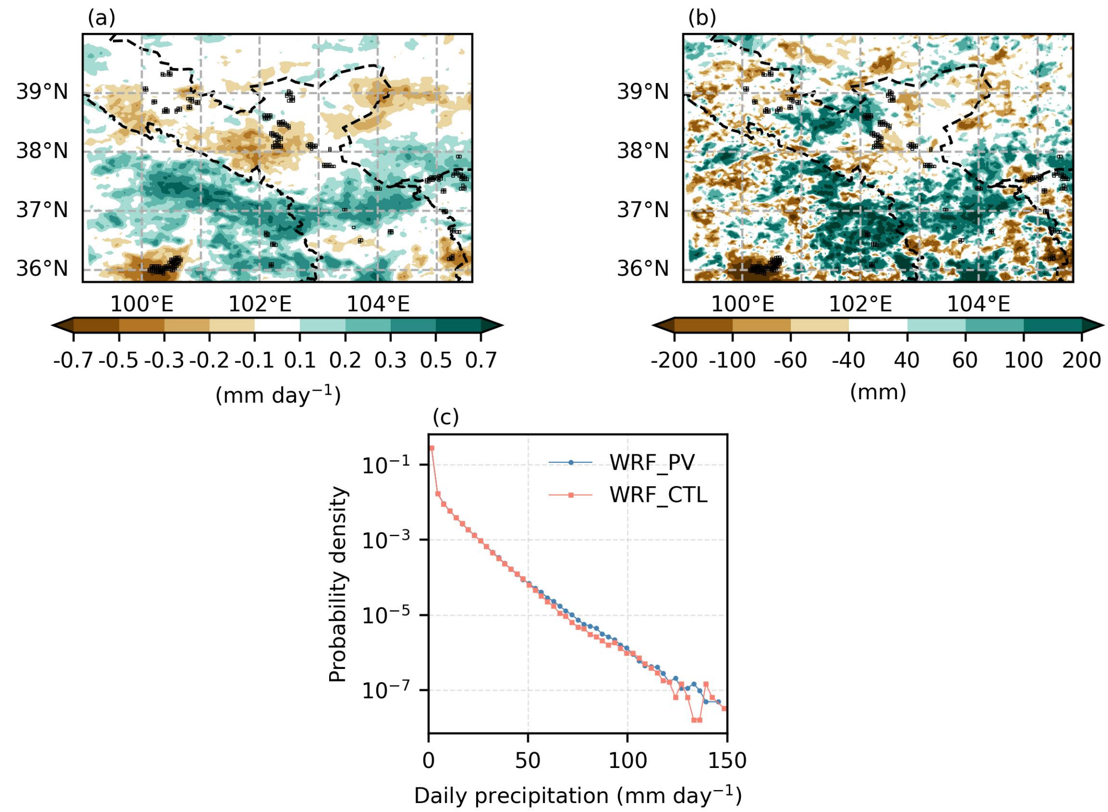

Figure R2.1: Spatial changes and probability density distributions of summer precipitation during 2018–2024. (a) Difference in mean daily precipitation between WRF_PV and WRF_CTL. (b) Difference in cumulative extreme precipitation (>30 mm day^{-1}) amount between WRF_PV and WRF_CTL. (c) Probability density distributions of daily precipitation intensity in WRF_PV and WRF_CTL over D03. In (a) and (b), grey grid symbols denote PV grid cells. (Figure 9 in the revised manuscript)

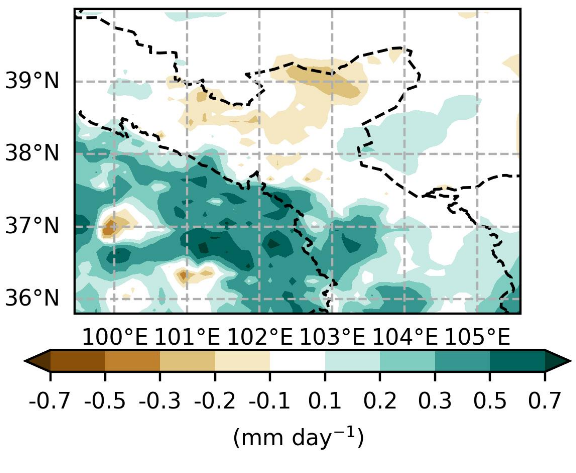

Figure R2.2: Difference in CMFD summer mean daily precipitation between 2018–2024 and 2000–2012. (Figure S1 in the supplement)

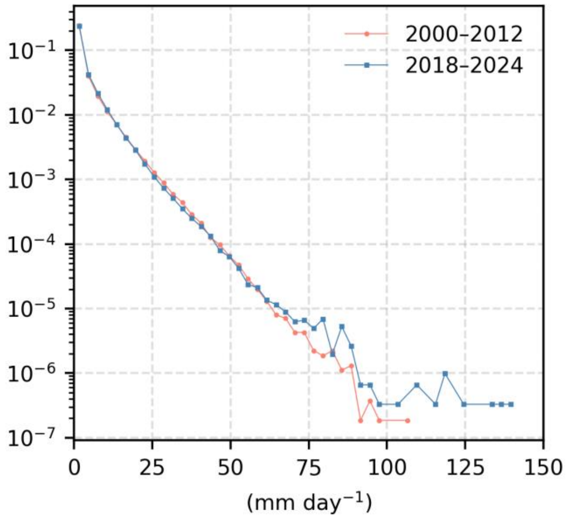

Figure R2.3: Probability density distributions of CMFD daily summer precipitation during 2000–2012 and 2018–2024. (Figure S2 in the supplement)

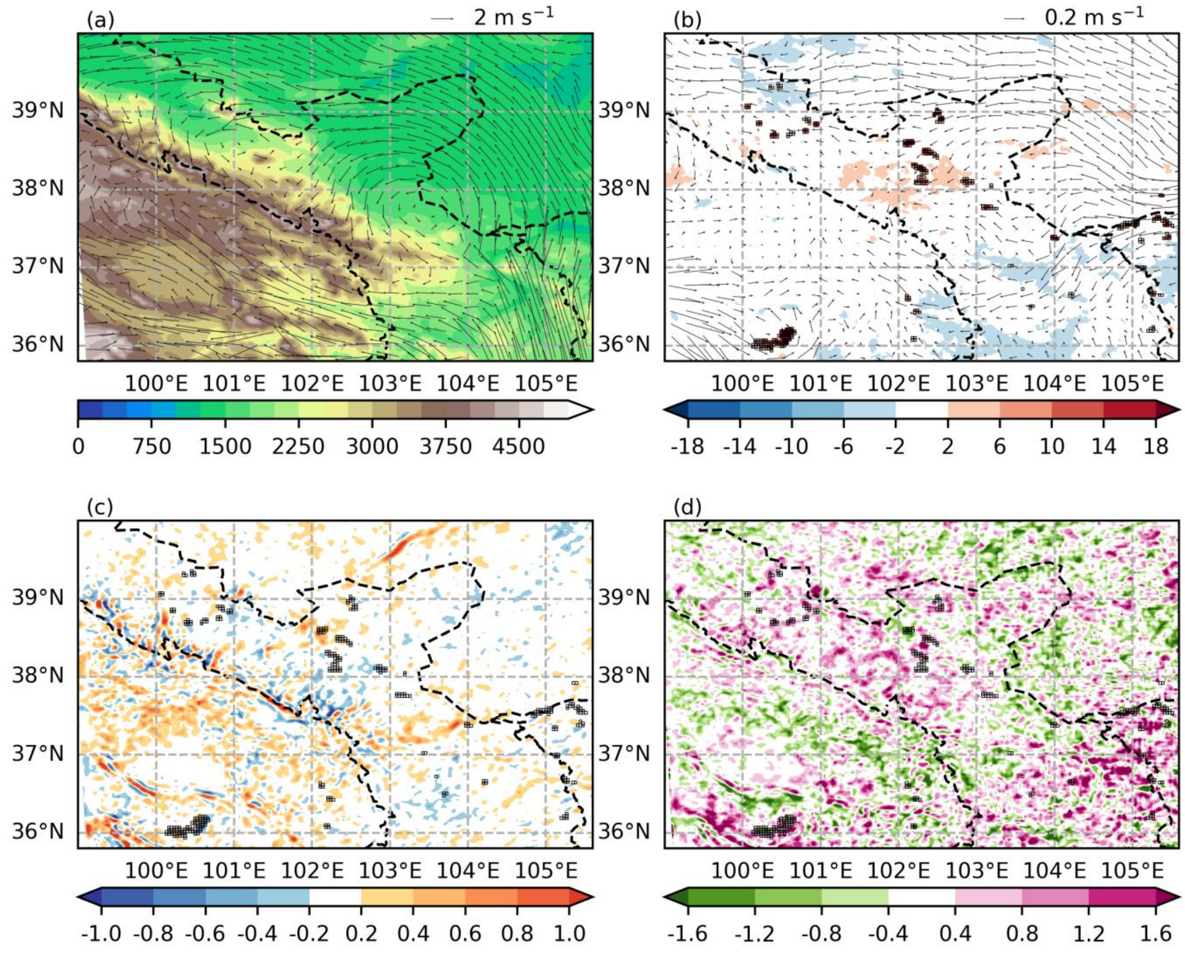

Figure R2.4: Terrain and atmospheric processes during the summers of 2018–2024. (a) Terrain height (m, shading) and near-surface wind field in WRF_CTL (vectors). (b) Differences in sensible heat flux (W m^{-2}, shading) and near-surface wind field (vectors). (c) Difference in vertical velocity (cm s^{-1}), with positive values indicating enhanced upward motion. (d) Difference in vertically integrated water vapor flux divergence (10^{-5} kg m^{-2} s^{-1}), with negative values indicating enhanced moisture convergence. All differences are calculated as WRF_PV minus WRF_CTL. In (b–d), grey grid symbols denote PV grid cells. (Figure 10 in the revised manuscript)

Table R2.2: Comparison of summer mean downward shortwave radiation between 2000–2012 and 2018–2024 based on CMFD. (Table S2 in the supplement)

Variable	2000–2012	2018–2024	Difference (later − earlier)	p value
Summer mean downward shortwave radiation (W m^{-2})	257.06	249.77	−7.29	0.047

The revised text reads:

"Figure 9 shows the spatial distributions of the changes in daily mean and cumulative extreme precipitation between WRF_PV and WRF_CTL together with the probability density distributions of daily precipitation. The domain-mean precipitation difference between WRF_PV and WRF_CTL was small, indicating little change in the overall summer precipitation amount (Fig. 9a). However, the spatial response was pronounced, with precipitation increasing mainly over the central and southern parts of the domain and decreasing over several northern and western areas. Despite only small changes in mean precipitation (Fig. 9a), the related changes in water vapor convergence, vertical motion, and precipitation were dynamically coherent (Fig. 10c and 10d). This precipitation response pattern was broadly consistent with the period difference in the reanalysis data (Fig. S1). Accumulated extreme precipitation showed a more distinct and localized spatial response than mean precipitation (Fig. 9b). The probability distributions of WRF_PV and WRF_CTL were generally similar for light and moderate rainfall. However, WRF_PV showed a slightly higher probability density for heavy rainfall of 60–100 mm day^{-1}, suggesting a modest shift toward more intense rainfall events (Fig. 9c). A broadly similar shift in the daily precipitation distribution was also evident between the two periods in the reference dataset (Fig. S2)."

"In order to understand the association of the changes in circulation and precipitation with the PV distribution, Figures 10a and 10b show the summer-mean low-level circulation and the change in sensible heat caused by PV deployment. The climatological low-level flow was predominantly southeasterly and closely influenced by the regional topography (Fig. 10a). The climatological precipitation field exhibited pronounced spatial heterogeneity, with higher precipitation over the plateau, where the low-level flow encountered rising terrain (Fig. 3a and 10a). Between 36° and 37° N, PV-induced sensible heating strengthened low-level convergence, accompanied by an enhanced easterly flow and water vapor transport toward the plateau (Fig. 10b). This circulation anomaly reinforced the existing terrain-related convergence and ascent (Fig. 10c and 10d), contributing to increased precipitation over northern Qinghai. Moreover, we take the area of extreme precipitation near 38.6° N, which is located well within the model domain and is largely free from lateral boundary effects, as an example (Fig. 9b). Increases in sensible heat flux were concentrated over the PV clusters and were accompanied by convergence in the low-level wind field (Fig. 10b). The easterly, southeasterly, and northeasterly wind anomalies flowed toward the PV clusters and ascended along the mountain range that marks the northern boundary of Gansu Province (Fig. 10a), inducing weak upward motion (Fig. 10c). Although this weak anomalous ascent led to only a slight modification of mean precipitation (Fig. 9a), it could produce enhanced extreme precipitation under appropriate conditions (Fig. 9b). These spatial correspondences suggested that PV-induced increases in sensible heat flux perturbed the local circulation, while the background flow and complex terrain modulated the locations of the resulting ascent, moisture convergence, and precipitation enhancement."

Location: Section 4.4, lines 409–441, Figs. 9–10, S1–S2, Table S2.

Comment 6: *Line 370: The statement is valid, but it is currently too brief and underdeveloped, given its importance. The authors should expand this discussion to more clearly articulate why a fully coupled land–atmosphere–ecosystem modeling framework is necessary for future work. In particular, PV installations can alter not only surface energy balance but also vegetation dynamics, soil moisture, and carbon fluxes. These processes may introduce additional feedbacks that are not captured in the* *current WRF-PV framework and could influence both local climate and longer-term ecosystem responses. The authors are encouraged to elaborate on (1) which key ecosystem processes are currently missing, (2) how their omission may affect the interpretation of the present results, and (3) how incorporating such processes in future model development could improve the robustness of PV–climate impact assessments. This would strengthen the discussion and better position the study within the broader context of land–climate interactions.*

Response: Thank you for this valuable suggestion. We agree that the original discussion did not sufficiently explain the need for a fully coupled land–atmosphere–ecosystem modeling framework. We have clarified that soil moisture evolved interactively in the Noah land-surface model in both WRF_CTL and WRF_PV and was therefore not held fixed. Nevertheless, the present study did not systematically diagnose the response of soil moisture.

Vegetation conditions were prescribed rather than dynamically simulated. Consequently, the present results primarily represent short-term physical responses to PV deployment and do not include longer-term vegetation-mediated feedbacks through transpiration, sensible–latent heat partitioning, and carbon exchange. We therefore identify the development of a fully coupled PV–land–atmosphere–ecosystem framework as an important direction for future work, particularly for assessing agrivoltaic applications in dryland regions.

The revised text reads:

> "The present analysis focused on surface energy balance and land–atmosphere responses. Although soil moisture evolved interactively in the Noah land-surface model, its response to PV-induced shading was not systematically diagnosed. Vegetation conditions were prescribed rather than dynamically simulated. Over longer time scales, PV-induced changes in radiation, soil moisture, and near-surface microclimate may affect vegetation activity, which could modify transpiration, sensible–latent heat partitioning, and carbon exchange (Barron-Gafford et al., 2025; Jia et al., 2026). Consequently, the present results mainly represent the short-term physical responses to PV deployment and do not fully capture these longer-term feedbacks. Therefore, future work should extend WRF-PV toward a fully coupled PV–land–atmosphere–ecosystem model that can represent indirect feedbacks through vegetation-mediated land–atmosphere exchange, thereby improving the robustness of PV–climate impact assessments. Such a framework would be useful for future agrivoltaic applications in dryland regions, where the climatic effects of panel shading are closely tied to soil moisture conservation and vegetation-mediated land–atmosphere exchange (Ruth et al., 2026)."

Location: Section 5, lines 500–510.

Comment 7: *Line 25: The introduction would benefit from a clearer articulation of the importance of PV system design in shaping climate impacts. At present, the discussion treats PV installations somewhat generically, but key design parameters, such as panel tilt angle, row spacing, orientation, tracking systems, and mounting height, strongly influence surface albedo, shading patterns, aerodynamic roughness, and heat exchange processes. These factors can modulate the magnitude and even the direction of PV-induced radiative and thermal effects.*

Response: Thank you for this helpful suggestion. We have expanded the Introduction to clarify that PV system design plays an important role in shaping the radiative and thermal effects of PV installations.

The revised text reads:

"Key PV system design parameters, such as panel tilt angle, row spacing, orientation, tracking systems, and mounting height, strongly influence surface albedo, shading patterns, and heat exchange processes (Smith et al., 2022; Stanislawski et al., 2022). These factors can modulate the magnitude and spatiotemporal characteristics of PV-induced radiative and thermal effects (Glick et al., 2020; Zainali et al., 2023)."

Location: Section 1, lines 41–45.

Comment 8: *The references appear to be not enough. Please update the literature cited to better position the work.*

Line 32: Barron-Gafford et al. "Agrivoltaics provide mutual benefits across the food–energy–water nexus in drylands." Nature Sustainability 2.9 (2019): 848-855.

Line 370: Jia et al. "Climate-driven divergence in biophysical and economic impacts of agrivoltaics.Proceedings of the National Academy of Sciences 123.10 (2026): e2514380123.

Ruth et al. "Enhancing climate-smart crop performance in arid agrivoltaics systems: effects of photovoltaic shading and soil amendments on tepary bean growth, yield, and associated soil microbiome." Plant and Soil (2026): 1-25.

Response: Thank you for this valuable suggestion. We have expanded the literature discussion and added the suggested studies on agrivoltaic water, vegetation, and ecosystem responses, including Barron-Gafford et al. (2019), Jia et al. (2026), and Ruth et al. (2026).

Location: Sections 1 and 5, lines 36, 504, 510.

Almukhtar, H., Lie, T. T., and Al-Shohani, W. A. M.: Comprehensive analysis of dust impact on photovoltaic module temperature: Experimental insights and mathematical modeling, Sol. Energy, 265, 112125, https://doi.org/10.1016/j.solener.2023.112125, 2023.

Armstrong, A., Ostle, N. J., and Whitaker, J.: Solar park microclimate and vegetation management effects on grassland carbon cycling, Environ. Res. Lett., 11, 074016, https://doi.org/10.1088/1748-9326/11/7/074016, 2016.

Armstrong, S. and Hurley, W. G.: A thermal model for photovoltaic panels under varying atmospheric conditions, Appl. Therm. Eng., 30, 1488–1495, https://doi.org/10.1016/j.applthermaleng.2010.03.012, 2010.

Barron-Gafford, G. A., Pavao-Zuckerman, M. A., Minor, R. L., Sutter, L. F., Barnett-Moreno, I., Blackett, D. T., Thompson, M., Dimond, K., Gerlak, A. K., Nabhan, G. P., and Macknick, J. E.: Agrivoltaics provide mutual benefits across the food–energy–water nexus in drylands, Nat. Sustain., 2, 848–855, https://doi.org/10.1038/s41893-019-0364-5, 2019.

Barron-Gafford, G. A., Murphy, P., Salazar, A., Lepley, K., Rouini, N., Barnett-Moreno, I., and Macknick, J. E.: Agrivoltaics as a climate-smart and resilient solution for midday depression in photosynthesis in dryland regions, npj Sustain. Agric., 3, 32, https://doi.org/10.1038/s44264-025-00073-1, 2025.

Broadbent, A. M., Krayenhoff, E. S., Georgescu, M., and Sailor, D. J.: The observed effects of utility-scale photovoltaics on near-surface air temperature and energy balance, J. Appl. Meteorol. Climatol., 58, 989–1006, https://doi.org/10.1175/JAMC-D-18-0271.1, 2019.

Chang, R., Luo, Y., and Zhu, R.: Simulated local climatic impacts of large-scale photovoltaics over the barren area of Qinghai, China, Renew. Energy, 145, 478–489, https://doi.org/10.1016/j.renene.2019.06.059, 2020.

Chang, R., Yan, Y., Luo, Y., Xiao, C., Wu, C., Jiang, J., and Shi, W.: A coupled WRF-PV mesoscale model simulating the near-surface climate of utility-scale photovoltaic plants, Sol. Energy, 245, 278–289, https://doi.org/10.1016/j.solener.2022.09.023, 2022.

Coll, C., Niclòs, R., Puchades, J., García-Santos, V., Perelló, M., and Pérez-Planells, L.: Demonstrating the suitability of the radiance-based method for assessing the accuracy of MODIS land surface temperature products, IEEE Trans. Geosci. Remote Sens., 62, 4412915, https://doi.org/10.1109/TGRS.2024.3454377, 2024.

Duffie, J. A. and Beckman, W. A.: Solar Engineering of Thermal Processes, 4th ed., John Wiley & Sons, Inc., https://doi.org/10.1002/9781118671603, 2013.

Fan, C. and Huang, X.: Satellite-observed changes of surface spectral reflectances due to solar farming and the implication for radiation budget, Environ. Res. Lett., 15, 114047, https://doi.org/10.1088/1748-9326/abbdea, 2020.

Fan, C. and Huang, X.: Direct impact of solar farm deployment on surface longwave radiation, Environ. Res. Commun., 3, 125006, https://doi.org/10.1088/2515-7620/ac40f1, 2021.

Ferrari Muniz, R., Silva Greatti, B., Sandrini, M., Paulo Belançon, M., Valcarenghi, R., Dosciatti Bini, R., and Santaella Zanuto, V.: Glass application in solar energy technology, in: Materials Science, vol. 13, edited by: Cristina Vasconcelos, H., IntechOpen, https://doi.org/10.5772/intechopen.1010177, 2025.

Glick, A., Smith, S. E., Ali, N., Bossuyt, J., Recktenwald, G., Calaf, M., and Cal, R. B.: Influence of flow direction and turbulence intensity on heat transfer of utility-scale photovoltaic solar farms, Sol. Energy, 207, 173–182, https://doi.org/10.1016/j.solener.2020.05.061, 2020.

Hasan, A., Alnoman, H., and Rashid, Y.: Impact of integrated photovoltaic-phase change material system on building energy efficiency in hot climate, Energy Build., 130, 495–505, https://doi.org/10.1016/j.enbuild.2016.08.059, 2016.

Heusinger, J., Broadbent, A. M., Sailor, D. J., and Georgescu, M.: Introduction, evaluation and application of an energy balance model for photovoltaic modules, Sol. Energy, 195, 382–395, https://doi.org/10.1016/j.solener.2019.11.041, 2020.

Heusinger, J., Broadbent, A. M., Krayenhoff, E. S., and Weber, S.: Adaptation of a photovoltaic energy balance model for rooftop applications, Build. Environ., 192, 107628, https://doi.org/10.1016/j.buildenv.2021.107628, 2021.

Hu, A., Levis, S., Meehl, G. A., Han, W., Washington, W. M., Oleson, K. W., Van Ruijven, B. J., He, M., and Strand, W. G.: Impact of solar panels on global climate, Nat. Clim. Change, 6, 290–294, https://doi.org/10.1038/nclimate2843, 2016.

Hulley, G. C., Hook, S. J., and Baldridge, A. M.: Investigating the effects of soil moisture on thermal infrared land surface temperature and emissivity using satellite retrievals and laboratory measurements, Remote Sens. Environ., 114, 1480–1493, https://doi.org/10.1016/j.rse.2010.02.002, 2010.

Hulley, G. C., Malakar, N. K., Islam, T., and Freepartner, R. J.: NASA's MODIS and VIIRS land surface temperature and emissivity products: A long-term and consistent Earth system data record, IEEE J. Sel. Top. Appl. Earth Obs. Remote Sens., 11, 522–535, https://doi.org/10.1109/JSTARS.2017.2779330, 2018.

Jia, M., Peng, B., Guan, K., Lawrence, D. M., DeLucia, E. H., Knapp, A. K., Barron-Gafford, G. A., Khanna, M., Lombardozzi, D. L., Sturchio, M. A., Kannenberg, S. A., Zhao, L., McCall, J., Tang, J., Bernacchi, C. J., Mwebaze, P., Majeed, F., Lee, D., and Time, A.: Climate-driven divergence in biophysical and economic impacts of agrivoltaics, Proc. Natl. Acad. Sci. USA, 123, e2514380123, https://doi.org/10.1073/pnas.2514380123, 2026.

Jiang, H., Lu, L., and Sun, K.: Experimental investigation of the impact of airborne dust deposition on the performance of solar photovoltaic modules, Atmos. Environ., 45, 4299–4304, https://doi.org/10.1016/j.atmosenv.2011.04.084, 2011.

Jiang, J., Gao, X., Lv, Q., Li, Z., and Li, P.: Observed impacts of utility-scale photovoltaic plant on local air temperature and energy partitioning in the barren areas, Renew. Energy, 174, 157–169, https://doi.org/10.1016/j.renene.2021.03.148, 2021.

Li, A., Liu, L., Li, S., Cui, X., Chen, X., and Cao, X.: Global photovoltaic solar panel dataset from 2019 to 2022, Sci. Data, 12, 637, https://doi.org/10.1038/s41597-025-04985-y, 2025a.

Li, B., Lei, C., Zhang, W., Olawoore, V. S., and Shuai, Y.: Numerical model study on influences of photovoltaic plants on local microclimate, Renew. Energy, 221, 119551, https://doi.org/10.1016/j.renene.2023.119551, 2024.

Li, B., Lei, C., Zhang, W., Xu, J., and Shuai, Y.: A numerical simulation study of microclimate in PV power plant using coupled WRF-PVCM, Energy, 317, 134529, https://doi.org/10.1016/j.energy.2025.134529, 2025b.

Li, G., Hernandez, R. R., Blackburn, G. A., Davies, G., Hunt, M., Whyatt, J. D., and Armstrong, A.: Ground-mounted photovoltaic solar parks promote land surface cool islands in arid ecosystems, Renew. Sustain. Energy Transit., 1, 100008, https://doi.org/10.1016/j.rset.2021.100008, 2021.

Li, P., Luo, Y., He, Z., Zheng, J., Xia, X., Liao, Z., and Gao, X.: A comparative study of the effects of photovoltaic power plants in desert and lake on the microclimate, Energy Rep., 10, 2128–2137, https://doi.org/10.1016/j.egyr.2023.08.064, 2023.

Li, Y., Kalnay, E., Motesharrei, S., Rivas, J., Kucharski, F., Kirk-Davidoff, D., Bach, E., and Zeng, N.: Climate model shows large-scale wind and solar farms in the Sahara increase rain and vegetation, Science, 361, 1019–1022, https://doi.org/10.1126/science.aar5629, 2018.

Li, Z., Zhao, Y., Luo, Y., Yang, L., Li, P., Jin, X., Jiang, J., Liu, R., and Gao, X.: A comparative study on the surface radiation characteristics of photovoltaic power plant in the Gobi desert, Renew. Energy, 182, 764–771, https://doi.org/10.1016/j.renene.2021.10.054, 2022.

Lin, G.: Photovoltaic dataset of China from 2013 to 2023 for ten years, https://doi.org/10.57760/sciencedb.15684, 2024.

Long, J., Lu, Z., Miller, P. A., Pongratz, J., Guan, D., Smith, B., Zhu, Z., Xu, J., and Zhang, Q.: Large-scale photovoltaic solar farms in the Sahara affect solar power generation potential globally, Commun. Earth Environ., 5, 11, https://doi.org/10.1038/s43247-023-01117-5, 2024.

Lu, Z., Zhang, Q., Miller, P. A., Zhang, Q., Berntell, E., and Smith, B.: Impacts of large-scale Sahara solar farms on global climate and vegetation cover, Geophys. Res. Lett., 48, e2020GL090789, https://doi.org/10.1029/2020GL090789, 2021.

Luque, A. and Hegedus, S.: Handbook of Photovoltaic Science and Engineering, 2nd edn., John Wiley & Sons, Chichester, UK, https://doi.org/10.1002/9780470974704, 2011.

Marion, B., Schaefer, R., Caine, H., and Sanchez, G.: Measured and modeled photovoltaic system energy losses from snow for Colorado and Wisconsin locations, Sol. Energy, 97, 112–121, https://doi.org/10.1016/j.solener.2013.07.029, 2013.

Masson, V., Bonhomme, M., Salagnac, J.-L., Briottet, X., and Lemonsu, A.: Solar panels reduce both global warming and urban heat island, Front. Environ. Sci., 2, https://doi.org/10.3389/fenvs.2014.00014, 2014.

Mattei, M., Notton, G., Cristofari, C., Muselli, M., and Poggi, P.: Calculation of the polycrystalline PV module temperature using a simple method of energy balance, Renew. Energy, 31, 553–567, https://doi.org/10.1016/j.renene.2005.03.010, 2006.

Neinavaz, E., Skidmore, A. K., and Darvishzadeh, R.: Effects of prediction accuracy of the proportion of vegetation cover on land surface emissivity and temperature using the NDVI threshold method, Int. J. Appl. Earth Obs. Geoinf., 85, 101984, https://doi.org/10.1016/j.jag.2019.101984, 2020.

Ruth, M., Kushwaha, P., Barron-Gafford, G. A., and Babst-Kostecka, A.: Enhancing climate-smart crop performance in arid agrivoltaics systems: Effects of photovoltaic shading and soil amendments on tepary bean growth, yield, and associated soil microbiome, Plant Soil, 519, 1795–1819, https://doi.org/10.1007/s11104-025-08247-z, 2026.

Salamanca, F., Georgescu, M., Mahalov, A., Moustaoui, M., and Martilli, A.: Citywide impacts of cool roof and rooftop solar photovoltaic deployment on near-surface air temperature and cooling energy demand, Bound.-Layer Meteorol., 161, 203–221, https://doi.org/10.1007/s10546-016-0160-y, 2016.

Shaner, M. R., Atwater, H. A., Lewis, N. S., and McFarland, E. W.: A comparative technoeconomic analysis of renewable hydrogen production using solar energy, Energy Environ. Sci., 9, 2354–2371, https://doi.org/10.1039/C5EE02573G, 2016.

Smith, S. E., Viggiano, B., Ali, N., Silverman, T. J., Obligado, M., Calaf, M., and Cal, R. B.: Increased panel height enhances cooling for photovoltaic solar farms, Appl. Energy, 325, 119819, https://doi.org/10.1016/j.apenergy.2022.119819, 2022.

Stanislawski, B. J., Harman, T., Silverman, T. J., Cal, R. B., and Calaf, M.: Row spacing as a controller of solar module temperature and power output in solar farms, J. Renew. Sustain. Energy, 14, 063702, https://doi.org/10.1063/5.0123641, 2022.

Sun, X., Silverman, T. J., Zhou, Z., Khan, M. R., Bermel, P., and Alam, M. A.: An optics-based approach to thermal management of photovoltaics: Selective-spectral and radiative cooling, IEEE J. Photovolt., 7, 566–574, https://doi.org/10.1109/JPHOTOV.2016.2646062, 2017.

Trigo, I. F., Boussetta, S., Viterbo, P., Balsamo, G., Beljaars, A., and Sandu, I.: Comparison of model land skin temperature with remotely sensed estimates and assessment of surface-atmosphere coupling, J. Geophys. Res. Atmos., 120, 12096–12111, https://doi.org/10.1002/2015JD023812, 2015.

Turney, D. and Fthenakis, V.: Environmental impacts from the installation and operation of large-scale solar power plants, Renew. Sustain. Energy Rev., 15, 3261–3270, https://doi.org/10.1016/j.rser.2011.04.023, 2011.

Wang, A., Barlage, M., Zeng, X., and Draper, C. S.: Comparison of land skin temperature from a land model, remote sensing, and in situ measurement, J. Geophys. Res. Atmos., 119, 3093–3106, https://doi.org/10.1002/2013JD021026, 2014.

Wang, X., Zhou, Q., Zhang, Y., Liu, X., Liu, J., Chen, S., Wang, X., and Wu, J.: Diurnal asymmetry effects of photovoltaic power plants on land surface temperature in Gobi deserts, Remote Sens., 16, 1711, https://doi.org/10.3390/rs16101711, 2024.

Wei, S., Ziegler, A. D., Qin, Y., Wang, D., Chen, Y., Yan, J., and Zeng, Z.: Small reduction in land surface albedo due to solar panel expansion worldwide, Commun. Earth Environ., 5, 474, https://doi.org/10.1038/s43247-024-01619-w, 2024.

Wu, C., Liu, H., Yu, Y., Zhao, W., Liu, J., Yu, H., and Yetemen, O.: Ecohydrological effects of photovoltaic solar farms on soil microclimates and moisture regimes in arid Northwest China: A modeling study, Sci. Total Environ., 802, 149946, https://doi.org/10.1016/j.scitotenv.2021.149946, 2022.

Xu, Z., Li, Y., Qin, Y., and Bach, E.: A global assessment of the effects of solar farms on albedo, vegetation, and land surface temperature using remote sensing, Sol. Energy, 268, 112198, https://doi.org/10.1016/j.solener.2023.112198, 2024.

Yang, Y., Lin, S., Lu, R., and Liu, X.: CPVPD-2024: A Chinese photovoltaic plant dataset derived via a topography-enhanced deep learning framework, Sci. Data, 12, 1601, https://doi.org/10.1038/s41597-025-05891-z, 2025.

Yin, H., Krayenhoff, E. S., Voogt, J., Heusinger, J., and Aliabadi, A. A.: Simulation of tilted rooftop photovoltaic panels at city scale: Novel measurements, model development, and application in WRF, J. Geophys. Res. Atmos., 130, e2024JD043133, https://doi.org/10.1029/2024JD043133, 2025.

Ying, J., Li, Z., Yang, L., Jiang, Y., Luo, Y., and Gao, X.: The characteristics and parameterizations of the surface albedo of a utility-scale photovoltaic plant in the Gobi Desert, Theor. Appl. Climatol., 151, 1469–1481, https://doi.org/10.1007/s00704-022-04337-5, 2023.

Yue, S., Guo, M., Zou, P., Wu, W., and Zhou, X.: Effects of photovoltaic panels on soil temperature and moisture in desert areas, Environ. Sci. Pollut. Res., 28, 17506–17518, https://doi.org/10.1007/s11356-020-11742-8, 2021.

Zainali, S., Ma Lu, S., Stridh, B., Avelin, A., Amaducci, S., Colauzzi, M., and Campana, P. E.: Direct and diffuse shading factors modelling for the most representative agrivoltaic system layouts, Appl. Energy, 339, 120981, https://doi.org/10.1016/j.apenergy.2023.120981, 2023.

Zhang, G., Wang, W., Zhan, H., Wu, F., Zhang, Z., Xue, P., Qiu, F., and Hou, W.: The variation characteristics of temperature and precipitation in Mogao Grottoes of Dunhuang in recent 30 years, Plateau Meteorol., 42, 1069–1077, https://doi.org/10.7522/j.issn.1000-0534.2022.00064, 2023.

Zhang, J., Wu, L., and Dong, W.: Land-atmosphere coupling and summer climate variability over East Asia, J. Geophys. Res., 116, D05117, https://doi.org/10.1029/2010JD014714, 2011.

Zhang, J., Li, Z., Tao, J., Ge, Y., Zhong, Y., Wang, Y., and Yan, B.: Observed impacts of ground-mounted photovoltaic systems on the microclimate and soil in an arid area of Gansu, China, Atmosphere, 15, 936, https://doi.org/10.3390/atmos15080936, 2024.

Zhang, X., Lan, P., Lu, Y., Li, J., Xu, H., Zhang, J., Lee, Y., Rhee, J. Y., Choy, K.-L., and Song, W.: Multifunctional antireflection coatings based on novel hollow silica–silica nanocomposites, ACS Appl. Mater. Interfaces, 6, 1415–1423, https://doi.org/10.1021/am405258d, 2014.

Zhang, X. and Xu, M.: Assessing the effects of photovoltaic powerplants on surface temperature using remote sensing techniques, Remote Sens., 12, 1825, https://doi.org/10.3390/rs12111825, 2020.